



TECHNISCHE
UNIVERSITÄT
WIEN

DIPLOMARBEIT

Parquet DΓA with self-consistent recalculation of the impurity vertex

ausgeführt am

Institut für Festkörperphysik
der Technischen Universität Wien

unter der Anleitung von

Univ. Prof. Dr. Karsten Held

und

Univ. Ass. Dr. Anna Kauch

durch

Felix Hörbinger

Datum

Unterschrift

Abstract

In this thesis, the first fully self-consistent implementation of the dynamical vertex approximation (D Γ A) in its parquet formulation was realized. The method provides a framework to treat non-local correlations in strongly correlated electron systems, which lead to some of the most interesting phenomena in solid-state physics. In this thesis, we give an introduction to the parquet-, Bethe-Salpeter- and Schwinger-Dyson-equations, which form the backbone of D Γ A. We further give a sketch of the parquet-solver used within this work, the **victory-code**. We then show how to extract the fully irreducible vertex, a key component of D Γ A, from two-particle Green's functions obtained in a CT-QMC solution of the local impurity problem. A special focus lies on the update of the impurity problem to achieve self-consistency at the level of the local one-particle Green's function. This (outer) self-consistency is found to be particularly important with the introduction of non-local interactions, as is shown for the case of the benzene molecule. We also present results for the two dimensional Hubbard model on the square lattice, where the outer self-consistency does not impact the solution in a significant way at the currently attainable parameters. Nevertheless, the results indicate possible $d_{x^2-y^2}$ -wave superconducting pairing in the two-dimensional Hubbard model.

Zusammenfassung

Im Rahmen dieser Arbeit wurde die erste völlig selbstkonsistente Implementierung der Dynamischen Vertex Approximation (D Γ A) durchgeführt. Diese Methode erlaubt die Behandlung nicht-lokaler Korrelationen in stark korrelierten Elektronensystemen, die zu einigen der interessantesten Phänomenen der Festkörperphysik führen. Wir stellen die zugrundeliegenden Gleichungen, die Parquet Gleichungen, vor und skizzieren den Aufbau des Programms **victory-code**, das zur Lösung der Parquet Gleichungen verwendet wurde. Wir zeigen, wie man den völlig irreduziblen Vertex, der eine wichtige Komponente der D Γ A bildet, von den Zweiteilchen Greenschen Funktionen erhält, die wiederum mittels CT-QMC von einem Störstellenmodell berechnet werden. Ein besonderer Fokus dieser Arbeit liegt auf der Neuberechnung des Störstellenmodells, sodass Selbstkonsistenz auf dem Niveau der lokalen Einteilchen Greenschen Funktion erreicht wird. Diese (äußere) Selbstkonsistenz hat sich als besonders wichtig bei nicht-lokalen Wechselwirkungen herausgestellt, wie sie für das Benzol-Molekül eingeführt wurden. Wir präsentieren außerdem Ergebnisse für das zweidimensionale Hubbard Modell auf einem quadratischen Gitter, wo die äußere Selbstkonsistenz das Ergebnis für die derzeit erreichbaren Parameter nicht stark beeinflusst. Dennoch deuten die Ergebnisse auf mögliche $d_{x^2-y^2}$ -Wellen Supraleitung im zweidimensionalen Hubbard Modell hin.

Contents

1	Introduction	3
1.1	Antiferromagnetism and $d_{x^2-y^2}$ superconductivity	4
1.2	Notations and definitions	6
1.2.1	Green's function	6
1.2.2	Two-particle Green's function	8
1.3	DMFT	10
1.3.1	Anderson Impurity Model	10
1.3.2	DMFT cycle	11
2	Parquet DΓA	13
2.1	Outline of the method	13
2.2	Underlying equations	16
2.2.1	Parquet equation	16
2.2.2	Bethe-Salpeter equation	18
2.2.3	Schwinger-Dyson equation	19
2.3	Extraction of the fully irreducible vertex of the impurity problem	21
2.3.1	Vertex asymptotics	23
2.3.2	Λ , analytically	25
2.4	Numerical solution of the parquet equations	25
2.4.1	Symmetries	27
2.4.2	Coarse graining	28
2.5	Inverse impurity model	28
2.5.1	Uniqueness of the solution	30
2.6	Similar methods	33
3	Results	34
3.1	Benzene	34
3.2	2D-Hubbard model	39
3.2.1	Magnetic and superconducting order	39

3.2.2	Comparison of methods	46
3.2.3	Computational cost	51
3.2.4	Convergence	51
4	Conclusion and outlook	52

Chapter 1

Introduction

Strong electronic correlations give rise to some of the most interesting phenomena in condensed matter physics. Their treatment still poses a great challenge as they fail to be described by the standard approaches to solid state physics such as the density functional theory. The topic of this thesis, the dynamical vertex approximation (D Γ A), provides a non-perturbative method within the framework of many-body theory. Electronic correlations are especially important in systems with partially filled d - and f -orbitals, which are spatially highly confined and thus lead to strong interactions between electrons occupying the same orbital. While in principle the Hamiltonian of such a system is easily written down, vast simplifications have to be made in order to have a chance of solving it. The Hubbard Hamiltonian [1] is given in second quantization as

$$H = - \sum_{i,j,\sigma} t_{ij} \hat{c}_{i\sigma}^\dagger \hat{c}_{j\sigma} + U \sum_i \hat{n}_{i\uparrow} \hat{n}_{i\downarrow}. \quad (1.1)$$

Here $\hat{c}_{i\sigma}^\dagger, \hat{c}_{i\sigma}$ are the creation and annihilation operators at site i and spin σ , and the occupation number operator is $\hat{n}_{i\sigma} = \hat{c}_{i\sigma}^\dagger \hat{c}_{i\sigma}$. The first term represents the kinetic energy and allows electrons to “hop” from one site to another, with the so-called hopping amplitude t_{ij} . The second term introduces the interaction U between two electrons when they are on the same site. Throughout this thesis, only single-band systems with nearest-neighbor hopping are considered although more realistic systems are possible for computationally less demanding methods. Despite its simplicity, the Hubbard model is able to describe a range of interesting phenomena such as the Mott metal-insulator transition [2] and possibly superconductivity in two-dimensional planes [3].

The dynamical mean field theory (DMFT) [4] enabled a big step forward in the successful description of some of these phenomena, for example the Mott metal-insulator transition. In DMFT, the local part of the correlations can be treated non-perturbatively

by mapping the lattice onto a single site and solving the resulting single-site Hamiltonian self-consistently. In principle, this simpler Hamiltonian can be solved exactly, albeit still not analytically, for example through Quantum Monte Carlo methods with only statistical error [5]. This, however, comes at the price of the complete neglect of non-local correlations, which lead to a variety of phenomena such as high-temperature superconductivity in cuprates [6] or quantum-critical points. DMFT can be extended to include non-local correlations in two different ways: In cluster-DMFT, the lattice is mapped onto a finite cluster of sites, again embedded in a self-consistently determined bath. Non-local correlations are accounted for only within the length scale of the cluster, which is heavily limited as the computational effort scales exponentially. The dynamical vertex approximation (DΓA) [7, 8], along with other methods, takes a different approach by extending the diagrammatics of DMFT. This way, correlations on all length scales are taken into account. See Ref. [9] for a review of diagrammatic extensions of DMFT.

1.1 Antiferromagnetism and $d_{x^2-y^2}$ superconductivity

One major characteristic of any kind of superconductivity is spontaneous symmetry breaking: The non-zero expectation value of the anomalous operator, $\langle \hat{c}_a \hat{c}_b \rangle \neq 0$ breaks the $U(1)$ gauge symmetry of the Hamiltonian, $\hat{c}_a \rightarrow e^{i\phi} \hat{c}_a$ [10]. While this is all the symmetry-breaking that occurs in conventional superconductors, in high- T_c unconventional superconductors the symmetry group of the order parameter is even more reduced. Besides translational symmetry, the Hubbard model on a square lattice has the symmetry group [11]

$$G = U(1) \times SU(2) \times T \times C_{4v},$$

namely gauge symmetry $U(1)$, spin-rotational symmetry $SU(2)$, time reversal symmetry T and the point group symmetry of the square lattice, C_{4v} , which contains reflections, inversion and, most importantly for the present discussion, rotations by $\frac{\pi}{2}$. The character table of C_{4v} is given in Table 1.1. A classification of the order parameters is possible depending on which symmetries are conserved.

A hint on which symmetries are broken comes from the BCS-gap equation for the gap-function and order parameter $\Delta_{\mathbf{k}}$ [12]

$$\Delta_{\mathbf{k}} = - \sum_{\mathbf{k}'} V_{\mathbf{k}\mathbf{k}'} \frac{\Delta_{\mathbf{k}'}}{2E_{\mathbf{k}}}. \quad (1.2)$$

	E	C_4	C_4^2	C_2'	C_2''
A_{1g}	1	1	1	1	1
A_{2g}	1	1	1	-1	-1
B_{1g}	1	-1	1	1	-1
B_{2g}	1	-1	1	-1	1
$E_u(x)$	1	0	-1	1	0
$E_u(y)$	1	0	-1	-1	0

Table 1.1: The character table of C_{4v} . E is unity, C_4 a rotation of $\frac{\pi}{2}$ in the plane and C_2' and C_2'' a rotation of π around the $y = 0$ and $x = y$ axes. As A and B denote one-dimensional irreducible representations, their effect on the order parameter can be read directly from the character table.

For conventional superconductors, where an attractive potential $V_{\mathbf{k}} < 0$ is mediated by phonons, solutions are possible without any sign changes in $\Delta_{\mathbf{k}}$. In cuprates, the BCS-interaction is believed to be due to the exchange of antiferromagnetic spin fluctuations [13]. The effective interaction $V_{\mathbf{k},\mathbf{k}'}$ between a pair of electrons is proportional to $\chi_m(\mathbf{q} = \mathbf{k} - \mathbf{k}')$, as shown in Ref. [14] from a random phase approximation (RPA) argument. At low temperatures and near half filling, the system realizes an antiferromagnetic state, manifested by a pronounced peak at $\chi_m(\pi, \pi)$. With doping, this peak shifts towards smaller transfer momentum in one direction.

The sum in the gap equation is thus dominated by $\mathbf{k}' = (\pi, \pi) - \mathbf{k}$ and a solution is possible when $\Delta_{(\pi,\pi)-\mathbf{k}} = -\Delta_{\mathbf{k}}$, that is it changes its sign upon rotation by $\frac{\pi}{2}$. Indeed, the superconducting order parameter in cuprates has been shown experimentally [15] to have the symmetry of the irreducible representation B_{1g} , which exhibits this change of sign upon rotation (see Table 1.1). In analogy to the isotropic continuous case, where this symmetry is realized by states with angular momentum $l = 2$, the B_{1g} states are more commonly referred to as $d_{x^2-y^2}$ or simply d -wave. The corresponding order parameter can be expressed as

$$\Delta_{\mathbf{k}} = \frac{\Delta_0}{2} (\cos(k_x) - \cos(k_y)). \quad (1.3)$$

1.2 Notations and definitions

1.2.1 Green's function

The Green's function is one of the key elements for the treatment of many-body systems as it is directly related to a variety of physical quantities such as the spectral function. In real time, the one-particle Green's function is defined in the Heisenberg-picture as

$$G_{12}(t_1, t_2) = -i\langle \mathcal{T} \hat{c}_1(t_1) \hat{c}_2^\dagger(t_2) \rangle, \quad (1.4)$$

where \hat{c}_1^\dagger creates a particle at compound index 1, which contains the remaining relevant properties such as spin and position, and \mathcal{T} is the time-ordering operator. For finite temperatures, we follow the Matsubara formalism and use imaginary time arguments by performing a "Wick rotation" $t \rightarrow -i\tau$. This avoids complex exponents when combining the Boltzmann factor $e^{\beta H}$ and the time-evolution operator e^{-iHt} . The one-particle Green's function in imaginary time is

$$G_{12}(\tau_1, \tau_2) = -\langle \mathcal{T} \hat{c}_1(\tau_1) \hat{c}_2^\dagger(\tau_2) \rangle. \quad (1.5)$$

From this, one can recover the values on the real time axis through an analytic continuation by such methods as the maximum entropy approach [16]. The expectation value can be explicitly calculated in an eigenbasis of the Hamiltonian with eigenfunctions $|n\rangle$. Without loss of generality, for $\tau_1 > \tau_2$ this spectral representation reads

$$G_{12}(\tau_1, \tau_2) \propto \sum_n e^{(\tau_1 - \tau_2 - \beta)E_n} \langle n | \hat{c}_1 e^{-(\tau_1 - \tau_2)H} \hat{c}_2^\dagger | n \rangle.$$

To avoid divergences for realistic systems with an arbitrarily large number of states $|n\rangle$ and arbitrarily large energies E_n , one has to ensure that the exponential suppresses the matrix element by restricting

$$\tau_1 - \tau_2 < \beta. \quad (1.6)$$

The cyclic property of the trace leads to another simplification: some rewriting and exchanging the two operators gives [17]

$$\text{Tr}[e^{(\tau_1 - \beta)H} \hat{c}_1 e^{(\beta - \tau_1)H} e^{-\beta H} \hat{c}_2^\dagger(\tau_2)] = \text{Tr}[e^{-\beta H} \hat{c}_2^\dagger(\tau_2) e^{(\tau_1 - \beta)H} \hat{c}_1 e^{(\beta - \tau_1)H}], \quad (1.7)$$

which is just the same as $G_{12}(\tau_1 - \beta, \tau_2)$ except for a sign coming from the permutation in the time ordering operator.

$$G_{12}(\tau_1, \tau_2) = -G_{12}(\tau_1 - \beta, \tau_2). \quad (1.8)$$

Because of time translational symmetry, only the difference between the two time arguments matters: $G_{12}(\tau_1, \tau_2) = G_{12}(\tau_1 - \tau_2)$. Combining equations (1.6) and (1.8), one can constrain the time domain to

$$0 < \tau < \beta. \quad (1.9)$$

In accordance with all of the above, the Fourier expansion of the Green's function is

$$G_{12}(\tau) = \frac{1}{\beta} \sum_n e^{-i\nu_n \tau} G_{12}(i\nu_n), \quad (1.10)$$

$$G_{12}(i\nu_n) = \int_0^\beta d\tau e^{i\nu_n \tau} G_{12}(\tau), \quad (1.11)$$

where, due to the antiperiodicity of the Green's function, only the fermionic Matsubara frequencies $\nu_n = \frac{\pi}{\beta}(2n + 1)$ are allowed. Similarly, the bosonic Matsubara frequencies, which play a role in two-particle Green's functions, are denoted as $\omega_n = \frac{2\pi n}{\beta}$.

1.2.1.1 Noninteracting Green's function

The noninteracting Green's function for the Hubbard model can be obtained by transforming the creation and annihilation operators to k-space

$$\hat{c}_j = \frac{1}{N} \sum_{\mathbf{k}} e^{-i\mathbf{k}r_j} \hat{c}_{\mathbf{k}}, \quad (1.12)$$

$$\hat{c}_j^\dagger = \frac{1}{N} \sum_{\mathbf{k}} e^{i\mathbf{k}r_j} \hat{c}_{\mathbf{k}}^\dagger, \quad (1.13)$$

where j is a site index and N the number of sites. The non-interacting Hubbard Hamiltonian is instantly diagonalized:

$$H = \sum_{\mathbf{k}\sigma} (\epsilon_{\mathbf{k}} - \mu) \hat{c}_{\mathbf{k}\sigma}^\dagger \hat{c}_{\mathbf{k}\sigma}, \quad (1.14)$$

where we introduced the chemical potential μ . Inserting the Hamiltonian into the definition of the Green's function, we find [18]

$$G_{\mathbf{k},\mathbf{k}'}^0(\tau) = \delta_{\mathbf{k},\mathbf{k}'} \frac{e^{-\tau(\epsilon_{\mathbf{k}} - \mu)}}{1 + e^{-\beta(\epsilon_{\mathbf{k}} - \mu)}}. \quad (1.15)$$

Finally, the Fourier transform from τ to $i\nu$ gives

$$G_{\mathbf{k}}^0(i\nu) = \frac{1}{i\nu - \epsilon_{\mathbf{k}} + \mu}. \quad (1.16)$$

In the two dimensional Hubbard model on the square lattice with nearest neighbor hopping t , the dispersion relation is

$$\epsilon_{\mathbf{k}} = -2t(\cos(k_x) + \cos(k_y)). \quad (1.17)$$

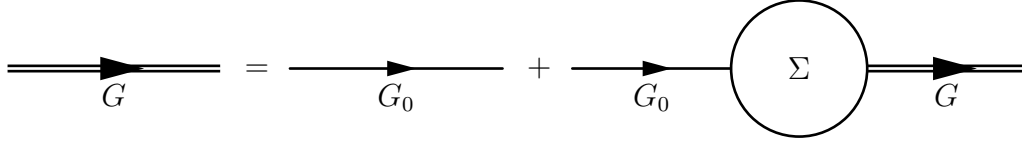


Figure 1.1: The Dyson equation. Double arrows denote the interacting Green's function.

1.2.1.2 Dyson equation

The Dyson equation systematically generates all one-particle diagrams from the non-interacting propagator and the self-energy, which consists of all one-particle irreducible diagrams. That means, these diagrams cannot be separated into two diagrams by cutting a line. Diagrammatically, the Dyson equation is shown in Fig. 1.1. It can easily be solved algebraically and reads

$$G_{\mathbf{k}}(i\nu)^{-1} = G_{\mathbf{k}}^0(i\nu)^{-1} - \Sigma_{\mathbf{k}}(i\nu). \quad (1.18)$$

Inserting the non-interacting Green's function from above gives

$$G_{\mathbf{k}}(i\nu) = \frac{1}{i\nu - \epsilon_{\mathbf{k}} + \mu - \Sigma_{\mathbf{k}}(i\nu)}. \quad (1.19)$$

1.2.2 Two-particle Green's function

Throughout this thesis, for two-particle quantities we follow the notations and sign conventions introduced in Ref. [19]

The two-particle Green's function plays an integral role in the present work. Its definition is

$$G_{1234}(\tau_1, \tau_2, \tau_3, \tau_4) = \langle \mathcal{T}_\tau [\hat{c}_1^\dagger(\tau_1) \hat{c}_2(\tau_2) \hat{c}_3^\dagger(\tau_3) \hat{c}_4(\tau_4)] \rangle. \quad (1.20)$$

Antiperiodicity and time domain are just as in the one-particle case and can be easily shown in the same manner.

In the noninteracting case, the operators in the expectation value simply contract according to Wick's theorem, giving the product of two one-particle propagators. When the interaction is turned on, an additional term arises where the two lines are connected by interactions. This term is encapsulated by the “full vertex” F as shown in Fig. 1.2. Note that the lines in these diagrams represent the interacting one-particle Green's function and thus already include self-energy insertions.

We further define the bare susceptibility

$$\chi_{0,1234}(\tau_1, \tau_2, \tau_3, \tau_4) = -G_{14}(\tau_1 - \tau_4)G_{32}(\tau_3 - \tau_2) \quad (1.21)$$

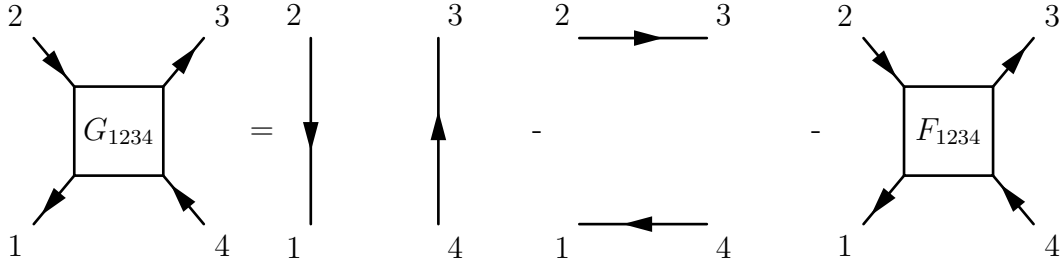


Figure 1.2: Diagrammatic representation of the two-particle Green's function. The generalized susceptibility is obtained from this by subtracting the first term on the right hand side.

and the generalized susceptibility,

$$\chi_{1234}(\tau_1, \tau_2, \tau_3, \tau_4) = G_{1234}(\tau_1, \tau_2, \tau_3, \tau_4) - G_{12}(\tau_1, \tau_2)G_{34}(\tau_3, \tau_4). \quad (1.22)$$

In the limit $\tau_2 \rightarrow \tau_1, \tau_4 \rightarrow \tau_3$, the latter gives the physical susceptibility which describes the linear response to a perturbation.

1.2.2.1 Frequency convention

The fourier transform of the two-particle Green's function or susceptibility is defined as

$$G_{1234}^{\nu_1\nu_2\nu_3\nu_4} = \int_0^\beta d\tau_1 d\tau_2 d\tau_3 d\tau_4 e^{-i(\nu_1\tau_1 - \nu_2\tau_2 + \nu_3\tau_3 - \nu_4\tau_4)} G_{1234}(\tau_1, \tau_2, \tau_3, \tau_4). \quad (1.23)$$

Due to time translational invariance, $\nu_1 - \nu_2 + \nu_3 - \nu_4 = 0$. The frequency dependence can thus be expressed by two fermionic frequencies ν, ν' and one bosonic frequency ω . The frequency conventions used in this work are depicted in Fig. 1.3. The same is true for the wave number \mathbf{k} due to translational symmetry or conservation of momentum, and combined indices $(k, k', q) \equiv (\nu, \mathbf{k}, \nu', \mathbf{k}', \omega, \mathbf{q})$ will be used when needed.

The transformation from particle-particle (pp) to particle-hole (ph) notation is given as

$$\begin{aligned} \omega_{ph} &= \omega_{pp} - \nu_{pp} - \nu'_{pp}, \\ \nu_{ph} &= \nu_{pp}, \\ \nu'_{ph} &= \nu'_{pp}. \end{aligned} \quad (1.24)$$

1.2.2.2 Spin dependence and SU(2) symmetry

In order for the expectation value in Eq. (1.20) to be non-zero, there has to be an equal number of creation and annihilation operators for each spin direction. Spin rotational

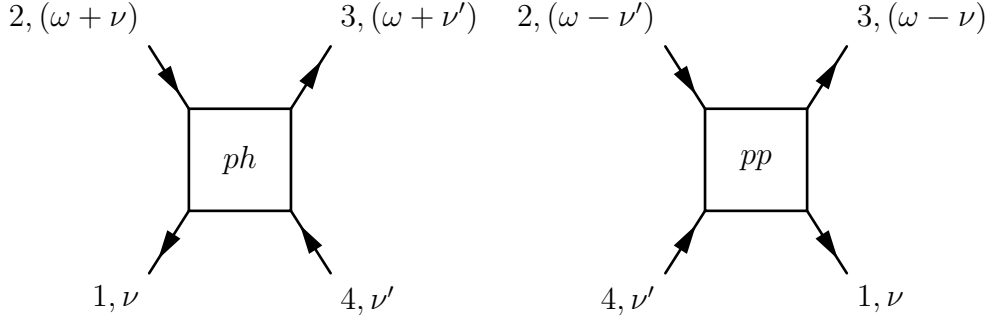


Figure 1.3: Particle-hole (left) and particle-particle (right) frequency- and momentum notation.

symmetry further reduces the number of independent combinations of spins to three, for which the following short notation is used:

$$\begin{array}{cccc}
 \sigma_1 & \sigma_2 & \sigma_3 & \sigma_4 \\
 \uparrow\uparrow & = & \uparrow & \uparrow & \uparrow & \uparrow \\
 \uparrow\downarrow & = & \uparrow & \uparrow & \downarrow & \downarrow \\
 \overline{\uparrow\downarrow} & = & \uparrow & \downarrow & \downarrow & \uparrow
 \end{array}$$

Symmetry when rotating spins by π dictates, for example, the following relation for the two-particle Green's function:

$$G_{2,\uparrow\downarrow} = G_{2,\downarrow\uparrow}. \quad (1.25)$$

Furthermore, rotation by $\frac{\pi}{2}$, that is replacing $\hat{c}_\uparrow^\dagger \rightarrow \frac{1}{\sqrt{2}}(\hat{c}_\uparrow^\dagger + \hat{c}_\downarrow^\dagger)$ and $\hat{c}_\downarrow^\dagger \rightarrow \frac{1}{\sqrt{2}}(\hat{c}_\uparrow^\dagger - \hat{c}_\downarrow^\dagger)$, leads to

$$G_{\overline{\uparrow\downarrow}} = G_{\uparrow\downarrow} - G_{\uparrow\uparrow}. \quad (1.26)$$

This relation holds not only for the two-particle Green's functions and susceptibilities, but also for the vertex functions.

1.3 DMFT

1.3.1 Anderson Impurity Model

To understand the dynamical mean field theory (DMFT), we first have to introduce the Anderson impurity model [20]. It contains one impurity site where electrons interact, embedded in a non-interacting bath. Its Hamiltonian is

$$H_{AIM} = -\mu(\hat{n}_\uparrow + \hat{n}_\downarrow) + U\hat{n}_\uparrow\hat{n}_\downarrow + \sum_{\mathbf{k},\sigma} \epsilon_{\mathbf{k},\sigma} \hat{c}_{\mathbf{k},\sigma}^\dagger \hat{c}_{\mathbf{k},\sigma} + \sum_{\mathbf{k},\sigma} V_{\mathbf{k}} (\hat{d}_\sigma^\dagger \hat{c}_{\mathbf{k},\sigma} + \hat{c}_{\mathbf{k},\sigma}^\dagger \hat{d}_\sigma). \quad (1.27)$$

The first two terms describe the chemical potential and the interaction when the impurity is occupied by two electrons. The third term gives the energy levels of the bath and the last one, often called hybridization term, introduces hopping between the impurity and the bath. In this notation, \hat{c}^\dagger creates an electron in the bath while \hat{d}^\dagger creates an impurity electron. The same holds for the annihilation operators and $\hat{n}_\sigma = \hat{d}_\sigma^\dagger \hat{d}_\sigma$ is the occupation on the impurity. Again, this Hamiltonian can be adapted to account for multi-orbital impurities yet in the present work only one-band calculations were done.

While a variety of methods to calculate expectation values such as the Green's function on the impurity are available, in this work a continuous-time quantum Monte Carlo (CT-QMC) solver [5] in the hybridization expansion [21], namely `w2dynamics` [22, 23, 24, 25], was used. The input to this method is the hybridization function $\Delta(i\nu)$, which encapsulates the properties of the bath

$$\Delta(i\nu) = \sum_{\mathbf{k}} \frac{V_{\mathbf{k}}^2}{i\nu - \epsilon_{\mathbf{k}}} . \quad (1.28)$$

1.3.2 DMFT cycle

The DMFT introduces the mapping of the lattice onto an impurity model in a self-consistently determined bath. The assumption made here is that the lattice self-energy is purely local and only composed of local lines. Self-consistency is achieved when these local lines are the same on the lattice and on the impurity,

$$G_{loc}(i\nu) = \sum_{\mathbf{k}} G(\mathbf{k}, i\nu) = G_{imp}(i\nu) , \quad (1.29)$$

where the second equation is the Dyson equation for the impurity. The self-energy enters the above expression through the Dyson-equation for the lattice Green's function, Eq. (1.19). Finally, we need to relate the hybridization function to the non-interacting Green's function on the impurity, $\mathcal{G}(i\nu)$, through

$$\Delta(i\nu) = i\nu - \mathcal{G}(i\nu)^{-1} + \mu = i\nu - G_{loc}(i\nu)^{-1} - \Sigma_{loc}(i\nu) + \mu. \quad (1.30)$$

The DMFT-cycle (see also Fig. 2.1) goes as follows:

1. Begin with some guess for the self-energy, for example the Hartree-term $\Sigma(i\nu) = \frac{U}{2}$.
2. Calculate the local lattice Green's function by summing Eq. (1.19) over the Brillouin zone.
3. Calculate the hybridization function Δ from Σ and G_{loc} through Eq. (1.30).

4. Compute the impurity Green's function from Δ using CT-QMC.
5. Extract the self-energy through the Dyson equation on the impurity, $\Sigma = \mathcal{G}^{-1} - G_{imp}^{-1}$.
6. Enter step 2. with the new self-energy and iterate until convergence.

DMFT not only serves to understand DFA conceptually, but also as the starting-point for the parquet DFA. Once the above cycle is converged, from the resulting hybridization function we calculate the two-particle Green's function and the fully irreducible vertex that enters the first iteration of the parquet DFA, as will be explained later.

Chapter 2

Parquet D Γ A

The dynamical vertex approximation (D Γ A) [7, 8] can be seen as a diagrammatic extension of DMFT. The assumption of the locality of the irreducible building block from which all relevant diagrams are generated is taken from the one-particle level in DMFT to the two-particle level in D Γ A. Instead of the Dyson-equation, the much more complicated parquet- and Bethe-Salpeter equations have to be applied to generate the reducible diagrams. The benefit of this increase in complexity and computational cost is the inclusion of non-local correlations on all length scales. Similar as for DMFT, the irreducible building block, called the fully irreducible vertex Λ , is obtained by mapping the lattice onto a self-consistently determined impurity and thus non-perturbatively.

2.1 Outline of the method

Before going into more detail for each step of the parquet D Γ A, this section aims to outline the whole method and compare it to DMFT where possible. To this end, Fig. 2.1 gives a direct comparison of the flow diagrams of both methods.

To start with the self-consistent parquet D Γ A cycle, we need some initial guess for the fully irreducible vertex Λ . Usually it is taken from a converged DMFT solution since this provides a good estimate at a relatively low computational cost. Diagrammatically, Λ_{DMFT} is composed of the local Green's function from DMFT, G_{local}^{DMFT} , which will be gradually replaced by $G_{local}^{D\Gamma A}$ through iteration (described later as outer self-consistency). Once the hybridization that solves DMFT is known, we calculate the two-particle Green's function and extract Λ_{DMFT} . As mentioned, throughout this work all calculations on the impurity were done using the CT-QMC solver `w2dynamics` [24].

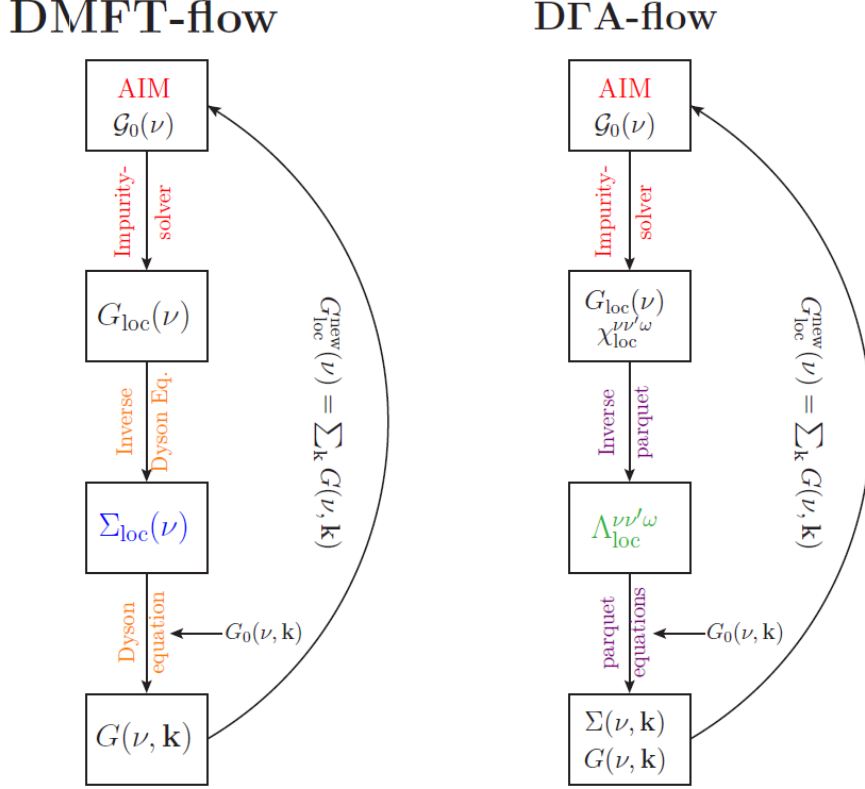


Figure 2.1: Flow diagrams comparing DMFT and DΓA. Taken from Ref. [19].

From Λ , the nonlocal full vertex $F^{kk'q}$ is generated through the Bethe-Salpeter and parquet equations. This process is depicted in Fig. 2.2. From the full vertex $F^{kk'q}$, one can calculate the non-local self-energy $\Sigma(k)$ through the Schwinger-Dyson equation of motion, which in turn generates the non-local Green's function through the Dyson equation. As the non-local Green's function was already required to solve the parquet equations, this whole procedure has to be iterated until self-consistency is achieved (described later as inner self-consistency). This step roughly resembles the much simpler use of the Dyson-equation in DMFT, which also generates all relevant diagrams for the local Green's function from its local building block, the self-energy. Throughout this work, the `victory-code` [26] was employed to handle this step.

Once the parquet equations are solved self-consistently, the first iteration of the parquet DΓA is completed. From here on, this will be referred to as one-shot DΓA and the required self-consistency as inner self-consistency. However, at that point the fully irreducible vertex is still calculated on an impurity model with the local Green's function from DMFT. To achieve the full outer self-consistency, one has to find a new impurity model with the local Green's function from DΓA. The whole cycle is then repeated until convergence, that is $G^{AIM} = G_{local}^{D\Gamma A}$.

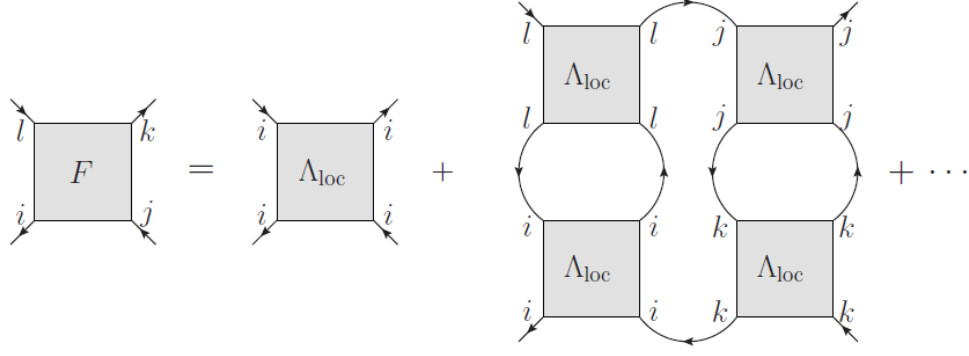


Figure 2.2: The nonlocal vertices are generated by connecting the local fully irreducible vertex by non-local one-particle propagators. Taken from Ref. [19].

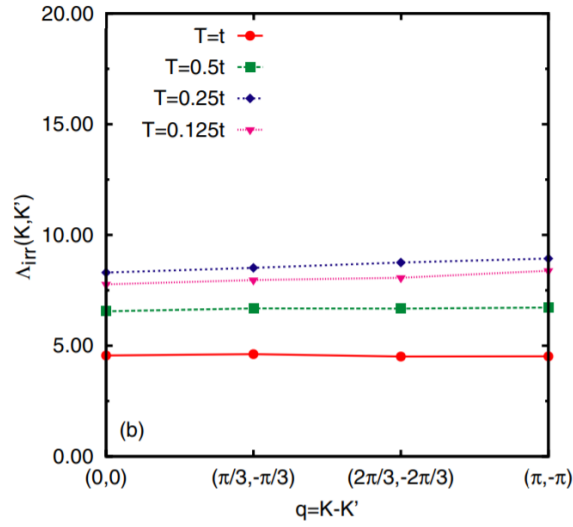


Figure 2.3: The almost non-existent k -dependence of the fully irreducible vertex in the 2D-Hubbard model with $U = 4t$ and $\langle n \rangle = 0.85$ calculated within the dynamical cluster approach on 24 sites by Maier et al. Taken from Ref. [27].

The key approximation in the parquet DGA is that the fully irreducible vertex Λ is composed only of local lines, and thus purely local itself. This can be shown diagrammatically to be accurate in infinite dimensions, as non-local contributions decay at least as $\frac{1}{\sqrt{Z}}$ where Z is the coordination number. It was found numerically in dynamical cluster approximation (DCA) calculations that already for the 2D-Hubbard model Λ is essentially purely local, as shown in Fig. 2.3.

The rest of this chapter aims to elaborate on each step of the fully self-consistent parquet DGA cycle.

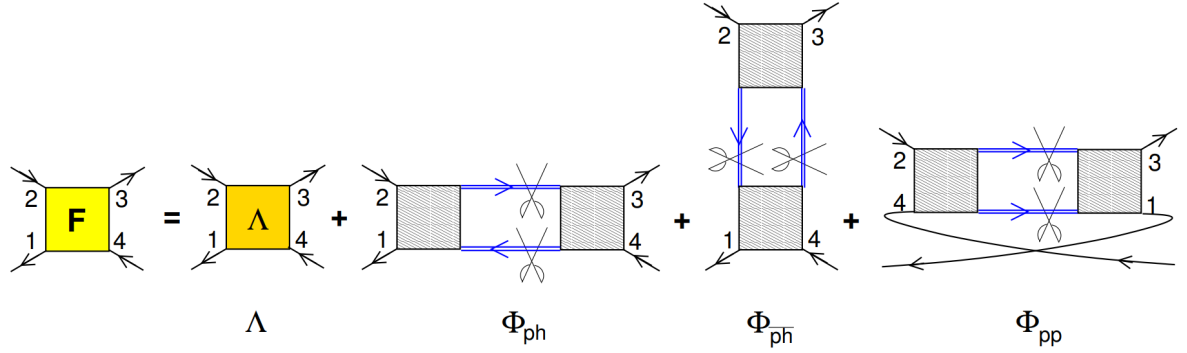


Figure 2.4: The parquet equation and the classification of reducible diagrams into the three channels ph , \overline{ph} and pp . Taken from Ref. [7].

2.2 Underlying equations

2.2.1 Parquet equation

While one-particle reducibility is easily defined - those diagrams that can be split into two by cutting a single one-particle propagator are one-particle reducible - some more thought has to be put into the reducibility of two-particle diagrams. First of all, let us note that connected two-particle diagrams cannot be one-particle reducible because they would violate conservation of particles, since there would necessarily be vertices with one more ingoing than outgoing line or vice versa.

Reducibility on the two-particle level is defined as follows: a diagram is two-particle reducible if it can be split into two diagrams by cutting two one-particle propagators. After cutting a diagram in two, there are three different ways in which the original legs can stay at the same diagram, leading to the definition of the three channels shown in Fig. 2.4, called particle-particle (pp), particle-hole longitudinal (ph) and particle-hole transversal (\overline{ph}).

At the heart of the parquet formalism lies the observation that any diagram is either fully irreducible or reducible in exactly one channel. This is easily seen by trying to construct a diagram that is reducible in two channels: whichever way the missing lines in Fig. 2.5 are connected, reducibility in one channel will be broken.

Before elaborating more on the parquet formalism, some more clarification on the notations used in this work is in order.

- Λ is the fully irreducible vertex. It contains all diagrams that are irreducible in all three channels.

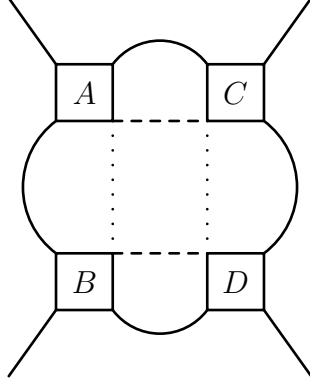


Figure 2.5: *Whichever way the the missing lines are connected (dashed or dotted), the diagram will only be reducible in one channel. Note that connecting one dashed and one dotted line results in a vertex with two incoming and one outgoing line, which is not possible for fermions.*

- Φ_{ch} contains all diagrams that are reducible in channel ch .
- Γ_{ch} contains all diagrams that are irreducible in channel ch .

This classification leads to the parquet equation,

$$F = \Lambda + \Phi_{ph} + \Phi_{\overline{ph}} + \Phi_{pp}. \quad (2.1)$$

From the above definitions further follow

$$\begin{aligned} F &= \Gamma_{ch} + \Phi_{ch} , \\ \Gamma_{ph} &= \Lambda + \Phi_{\overline{ph}} + \Phi_{pp} , \\ \Gamma_{pp} &= \Lambda + \Phi_{\overline{ph}} + \Phi_{ph} . \end{aligned} \quad (2.2)$$

For the ph - and pp -channel, the corresponding frequency and momentum conventions introduced in Fig. 1.3 are used. Let us now introduce these formulas with all their spin, frequency and momentum dependencies. The indices k and k' are used for combined fermionic frequency and momentum, q for the bosonic ones. Diagrammatically, the parquet equation is shown in Fig. 2.4. By applying the crossing symmetry, the \overline{ph} channel can be transformed into ph and thus does not have to be treated explicitly. This is demonstrated for the lowest order reducible diagram in both channels in Fig. 2.6. By exchanging particles 2 and 4 in the \overline{ph} -diagram, the two diagrams become equivalent and therefore, after adjusting the momentum argument accordingly,

$$\Phi_{ph\sigma\sigma'}^{kk'q} = -\Phi_{ph\sigma\sigma'}^{k(k+q)(k'-k)}, \quad (2.3)$$

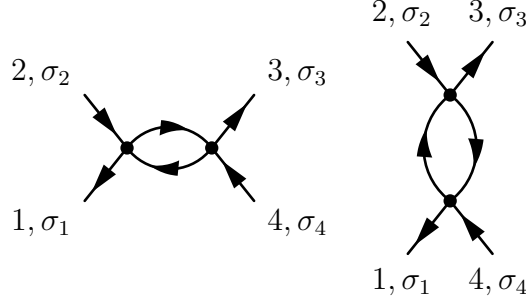


Figure 2.6: Equivalence between particle-hole and particle-hole transverse channel with exchanging two lines, shown for the lowest order diagrams in each channel.

where the exchange of the particle changes the order of spins from $\uparrow\downarrow$ to $\uparrow\downarrow$, but naturally $\overline{\uparrow\uparrow} = \uparrow\uparrow$.

Similarly, one has to exchange a line and shift frequencies to unify the notation for particle-hole and particle-particle channels. The equations for the irreducible vertices then read explicitly

$$\Gamma_{ph,\sigma\sigma'}^{kk'q} = \Lambda_{ph,\sigma\sigma'}^{kk'q} - \Phi_{ph,\sigma\sigma'}^{k(k+q)(k'-k)} - \Phi_{pp,\sigma\sigma'}^{kk'(k+k'+q)}, \quad (2.4)$$

$$\Gamma_{pp,\sigma\sigma'}^{kk'q} = \Lambda_{pp,\sigma\sigma'}^{kk'q} - \Phi_{ph,\sigma\sigma'}^{kk'(q-k-k')} + \Phi_{ph,\sigma\sigma'}^{k(q-k')(k'-k)}. \quad (2.5)$$

Note that the fully irreducible vertex Λ is channel-independent and the subscript ph or pp only denotes the notation, while for the irreducible Γ and reducible Φ it denotes channel and notation.

2.2.2 Bethe-Salpeter equation

The Bethe-Salpeter equation relates the irreducible vertex with the full one. Schematically it reads

$$F = \Gamma_{ch} + \Gamma_{ch}(GG)_{ch}F, \quad (2.6)$$

where $(GG)_{ch}$ denotes a connection by two single-particle propagators according to the respective channel, as demonstrated in Fig. 2.7 for the particle-hole channel. Algebraically, these equations are

$$F_{ph\uparrow\uparrow}^{kk'q} = \Gamma_{ph\uparrow\uparrow}^{kk'q} + \frac{1}{\beta} \sum_{k_1\sigma_1} \Gamma_{ph\uparrow\sigma_1}^{kk_1q} G(k_1) G(k_1 + q) F_{ph\sigma_1\uparrow}^{k_1k'q}, \quad (2.7)$$

$$F_{ph\uparrow\downarrow}^{kk'q} = \Gamma_{ph\uparrow\downarrow}^{kk'q} + \frac{1}{\beta} \sum_{k_1\sigma_1} \Gamma_{ph\uparrow\sigma_1}^{kk_1q} G(k_1) G(k_1 + q) F_{ph\sigma_1\downarrow}^{k_1k'q}. \quad (2.8)$$

One can decouple these two equations by adding or subtracting them and applying spin rotational symmetry, leading to the definition of the following quantities:

$$X_d = X_{\uparrow\uparrow} + X_{\uparrow\downarrow}, \quad (2.9)$$

$$X_m = X_{\uparrow\uparrow} - X_{\uparrow\downarrow} = X_{\uparrow\downarrow}, \quad (2.10)$$

where X represents F , Γ , Φ , Λ or χ .

In the particle-particle channel, the situation is similar and the equations read

$$F_{pp\uparrow\uparrow}^{kk'q} = \Gamma_{pp\uparrow\uparrow}^{kk'q} + \frac{1}{2\beta} \sum_{k_1} \Gamma_{pp\uparrow\uparrow}^{k_1k'q} G(k_1) G(q - k_1) F_{pp\uparrow\uparrow}^{k(q-k_1)q}, \quad (2.11)$$

$$F_{pp\uparrow\downarrow}^{kk'q} = \Gamma_{pp\uparrow\downarrow}^{kk'q} - \frac{1}{2\beta} \sum_{k_1\sigma_1} \Gamma_{pp\sigma_1\uparrow(-\sigma_1)\downarrow}^{k_1k'q} G(k_1) G(q - k_1) F_{pp\uparrow\sigma_1\downarrow(-\sigma_1)}^{k(q-k_1)q}, \quad (2.12)$$

$$F_{pp\uparrow\downarrow}^{kk'q} = \Gamma_{pp\uparrow\downarrow}^{kk'q} - \frac{1}{2\beta} \sum_{k_1\sigma_1} \Gamma_{pp\sigma_1\downarrow(-\sigma_1)\uparrow}^{k_1k'q} G(k_1) G(q - k_1) F_{pp\uparrow\sigma_1\downarrow(-\sigma_1)}^{k(q-k_1)q}. \quad (2.13)$$

For the notation of the spin dependencies and their symmetry relations, see Sec. 1.2.2.2. The factor $\frac{1}{2}$ serves to compensate double counting, as the two particle lines connecting F and Γ are indistinguishable [28]. The sign can be obtained from a comparison with the lowest order perturbative contributions. Due to the conservation of spin, Eq. (2.11) is already decoupled. Addition of the remaining two equations leads to (for X again representing F , Γ , Φ , Λ or χ)

$$X_s = X_{\uparrow\downarrow} - X_{\uparrow\downarrow} = 2X_{\uparrow\downarrow} - X_{\uparrow\uparrow}, \quad (2.14)$$

$$X_t = X_{\uparrow\downarrow} + X_{\uparrow\downarrow} = X_{\uparrow\uparrow}. \quad (2.15)$$

With $\chi_{0,ph}^{k,q} = -\beta G(k)G(k+q)$, and $\chi_{0,pp}^{k,q} = -\beta G(k)G(q-k)$, the decoupled Bethe-Salpeter equations then read [19]

$$F_{d,m}^{kk'q} = \Gamma_{d,m}^{kk'q} - \frac{1}{\beta^2} \sum_{k_1} \Gamma_{d,m}^{kk_1q} \chi_{0,ph}^{k_1q} F_{d,m}^{k_1k'q}, \quad (2.16)$$

$$F_s^{kk'q} = \Gamma_s^{kk'q} + \frac{1}{2\beta^2} \sum_{k_1} \Gamma_s^{kk_1q} \chi_{0,pp}^{k_1q} F_s^{k_1k'q}, \quad (2.17)$$

$$F_t^{kk'q} = \Gamma_t^{kk'q} - \frac{1}{2\beta^2} \sum_{k_1} \Gamma_t^{kk_1q} \chi_{0,pp}^{k_1q} F_t^{k_1k'q}. \quad (2.18)$$

2.2.3 Schwinger-Dyson equation

The Schwinger-Dyson equation relates the two-particle vertex F to the self-energy and thus to the one-particle Green's function. To derive it, one can start from the derivative of the one-particle Green's function with respect to time [29]

$$\frac{\partial G_{ij,\uparrow}(\tau)}{\partial \tau} = -\frac{\partial}{\partial \tau} \langle \mathcal{T} \hat{c}_{i,\uparrow}(\tau) \hat{c}_{j,\uparrow}^\dagger \rangle = -\delta(\tau) (\hat{c}_{j,\uparrow}^\dagger \hat{c}_{i,\uparrow} + \hat{c}_{i,\uparrow} \hat{c}_{j,\uparrow}^\dagger) - \langle \mathcal{T} \frac{\partial \hat{c}_{i,\uparrow}(\tau)}{\partial \tau} \hat{c}_{j,\uparrow}^\dagger \rangle, \quad (2.19)$$

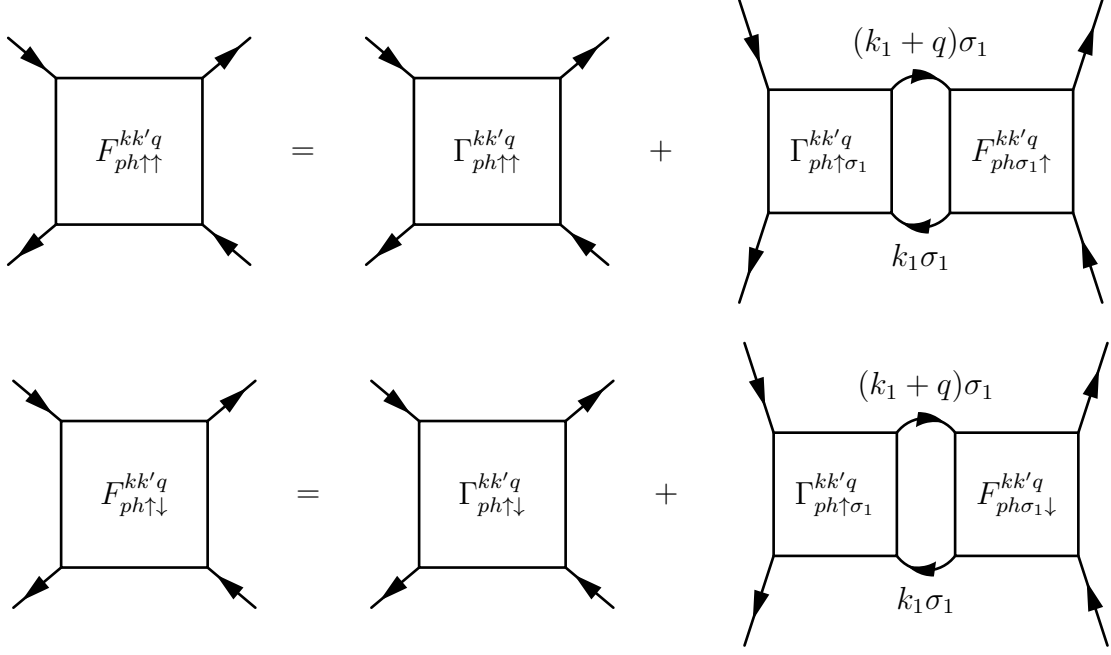


Figure 2.7: Bethe salpeter equation for the particle hole channel. k_1 and σ_1 are summed over.

where the first term on the right hand side comes from the derivative of the time-ordering operator. According to the Fermi-algebra, this term gives $-\delta(\tau)\delta_{ij}$. For the second term, the Heisenberg equation is [30]

$$\frac{\partial \hat{c}_{i,\uparrow}(\tau)}{\partial \tau} = [H, \hat{c}_{i,\uparrow}](\tau). \quad (2.20)$$

The Hamiltonian that we consider can be written as

$$H = \sum_{l,m,\sigma} H_{lm}^0 \hat{c}_{l,\sigma}^\dagger \hat{c}_{m,\sigma} + \sum_l U \hat{c}_{l,\uparrow}^\dagger \hat{c}_{l,\uparrow} \hat{c}_{l,\downarrow}^\dagger \hat{c}_{l,\downarrow}, \quad (2.21)$$

with the non-interacting part H^0 . To resolve the commutators emerging from Eq. (2.20), they first have to be converted to anticommutators and subsequently handled with the Fermi-algebra. This is done via the relations

$$[AB, C] = A[B, C] + [A, C]B = A\{B, C\} - \{A, C\}B, \quad (2.22)$$

$$\begin{aligned} [ABXY, C] &= [AB, C]XY + AB[XY, C] = \\ &= (A\{B, C\} - \{A, C\}B)XY + AB(X\{Y, C\} - \{X, C\}Y). \end{aligned} \quad (2.23)$$

The result is

$$\frac{\partial \hat{c}_{i,\uparrow}(\tau)}{\partial \tau} = \sum_m H_{mi}^0 \hat{c}_{m,\uparrow}(\tau) + U \hat{c}_{i,\downarrow}^\dagger(\tau) \hat{c}_{i,\downarrow}(\tau) \hat{c}_{i,\uparrow}(\tau), \quad (2.24)$$

$$\frac{\partial G_{ij,\uparrow}(\tau)}{\partial \tau} = \delta(\tau)\delta_{ij} + \sum_m H_{im}^0 G_{mj,\uparrow}(\tau) - U \langle \mathcal{T} [\hat{c}_{j,\uparrow}^\dagger(0) \hat{c}_{i,\uparrow}(\tau) \hat{c}_{i,\downarrow}^\dagger(\tau) \hat{c}_{i,\downarrow}(\tau)] \rangle, \quad (2.25)$$

where the last term can be written as a two-particle Green's function

$$\langle \mathcal{T} [\hat{c}_{j,\uparrow}^\dagger(0) \hat{c}_{i,\uparrow}(\tau) \hat{c}_{i,\downarrow}^\dagger(\tau) \hat{c}_{i,\downarrow}(\tau)] \rangle = G_{2,\uparrow\downarrow,jiii}(-\tau, 0, 0). \quad (2.26)$$

The Fourier Transform of Eq. (2.25) is, employing the particle-hole notation from Fig. 1.3 for the two-particle term,

$$(i\nu - H^0(\mathbf{k})) G_\uparrow(\nu, \mathbf{k}) = 1 + \sum_{\nu', \omega, \mathbf{k}', \mathbf{q}} G_{2,\uparrow\downarrow}(\nu, \nu', \omega, \mathbf{k}, \mathbf{k}', \mathbf{q}). \quad (2.27)$$

To connect this equation to the self-energy, we also take the time-derivative of the Dyson-equation. This is again easier in Fourier space by replacing $\frac{\partial}{\partial \tau} \rightarrow i\nu$. We further take into account that the non-interacting Green's function is a mathematical Green's function of the equation of motion [31]:

$$(i\nu - H^0(\mathbf{k})) G_\uparrow^0(\nu, \mathbf{k}) = 1. \quad (2.28)$$

Thus the above operator acting on the interacting Green's function gives

$$\begin{aligned} (i\nu - H^0(\mathbf{k})) G_\uparrow(\nu, \mathbf{k}) &= (i\nu - H^0(\mathbf{k})) (G_\uparrow^0(\nu, \mathbf{k}) + G_\uparrow^0(\nu, \mathbf{k}) \Sigma_\uparrow(\nu, \mathbf{k}) G_\uparrow(\nu, \mathbf{k})) \\ &= 1 + \Sigma_\uparrow(\nu, \mathbf{k}) G_\uparrow(\nu, \mathbf{k}). \end{aligned} \quad (2.29)$$

Comparing equations (2.27) and (2.29), we can identify

$$\Sigma(k) G(k) = -U \sum_{k', q} G_{2,\uparrow\downarrow}(k, k', q). \quad (2.30)$$

where the combined indices k, k', q now contain momentum and frequency. We further insert the relation between G_2 and the vertex F to finally get the expression for the Schwinger-Dyson equation,

$$\Sigma(k) = \frac{U \langle n \rangle}{2} + U \sum_{k', q} G(k+q) G(k') G(k'+q) F_{\uparrow\downarrow}^{k, k', q}. \quad (2.31)$$

It is shown diagrammatically in Fig. 2.8.

2.3 Extraction of the fully irreducible vertex of the impurity problem

The great advantage of mapping the lattice model onto an impurity model lies in the fact that the local problem can in principle be solved exactly. The CT-QMC solver `w2dynamics` [22, 24] can be configured to calculate the one-particle Green's function as

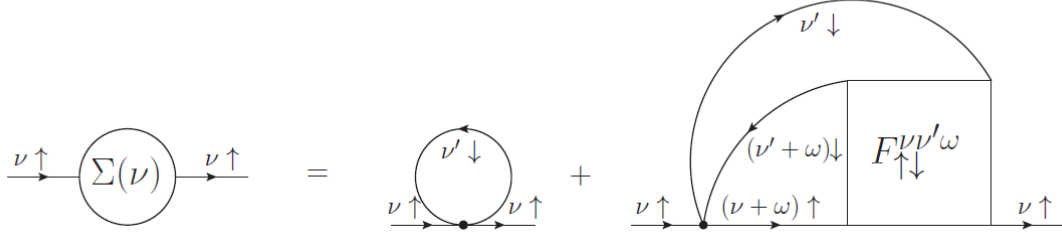


Figure 2.8: Diagrammatic representation of the Schwinger-Dyson equation. Taken from Ref. [19].

well as the generalized susceptibility in both ph - and pp -notation, from which the fully irreducible vertex can then be extracted in two steps: First we invert the local Bethe-Salpeter equation to get the irreducible vertices Γ . Then the fully irreducible vertex Λ can be calculated algebraically through the parquet equations. Let us discuss these steps in some more detail now:

For each bosonic frequency ω , the Bethe-Salpeter equation (2.16) can be interpreted as a matrix multiplication, thus enabling its solution for Γ through matrix inversion in the remaining indices ν_1, ν' . For the ph -channel, one gets

$$\Gamma_{d,m}^{\nu\nu_1,\omega} = \sum_{\nu'} F_{d,m}^{\nu\nu',\omega} [(\mathbb{1} - \frac{1}{\beta^2} \chi_{0,ph} F_{d,m})^{-1}]^{\nu_1\nu',\omega}. \quad (2.32)$$

Similarly, for the pp -channel

$$\Gamma_s^{\nu\nu_1,\omega} = \sum_{\nu'} F_s^{\nu\nu',\omega} [(\mathbb{1} + \frac{1}{2\beta^2} \chi_{0,pp} F_s)^{-1}]^{\nu_1\nu',\omega}, \quad (2.33)$$

$$\Gamma_t^{\nu\nu_1,\omega} = \sum_{\nu'} F_t^{\nu\nu',\omega} [(\mathbb{1} - \frac{1}{2\beta^2} \chi_{0,pp} F_t)^{-1}]^{\nu_1\nu',\omega}. \quad (2.34)$$

The reducible vertex Φ is calculated in each channel by $\Phi = F - \Gamma$ and finally the parquet equations can be solved for Λ :

$$\Lambda_d^{\nu\nu'\omega} = \Gamma_d^{\nu\nu'\omega} + \frac{1}{2} \Phi_d^{\nu(\nu+\omega)(\nu'-\nu)} + \frac{3}{2} \Phi_m^{\nu(\nu+\omega)(\nu'-\nu)} - \frac{1}{2} \Phi_s^{\nu\nu'(\nu+\nu'+\omega)} - \frac{3}{2} \Phi_t^{\nu\nu'(\nu+\nu'+\omega)}, \quad (2.35)$$

$$\Lambda_m^{\nu\nu'\omega} = \Gamma_m^{\nu\nu'\omega} + \frac{1}{2} \Phi_d^{\nu(\nu+\omega)(\nu'-\nu)} - \frac{1}{2} \Phi_m^{\nu(\nu+\omega)(\nu'-\nu)} + \frac{1}{2} \Phi_s^{\nu\nu'(\nu+\nu'+\omega)} - \frac{1}{2} \Phi_t^{\nu\nu'(\nu+\nu'+\omega)}, \quad (2.36)$$

$$\Lambda_s^{\nu\nu'\omega} = \Gamma_s^{\nu\nu'\omega} - \frac{1}{2} \Phi_d^{\nu\nu'(\omega-\nu-\nu')} + \frac{3}{2} \Phi_m^{\nu\nu'(\omega-\nu-\nu')} - \frac{1}{2} \Phi_d^{\nu(\omega-\nu')(\nu'-\nu)} + \frac{3}{2} \Phi_m^{\nu(\omega-\nu')(\nu'-\nu)}, \quad (2.37)$$

$$\Lambda_t^{\nu\nu'\omega} = \Gamma_t^{\nu\nu'\omega} - \frac{1}{2} \Phi_d^{\nu\nu'(\omega-\nu-\nu')} - \frac{1}{2} \Phi_m^{\nu\nu'(\omega-\nu-\nu')} + \frac{1}{2} \Phi_d^{\nu(\omega-\nu')(\nu'-\nu)} + \frac{1}{2} \Phi_m^{\nu(\omega-\nu')(\nu'-\nu)}. \quad (2.38)$$

Since the fully irreducible vertex is in principle not channel-specific, only two of these four quantities are independent, in accordance with the two independent spin combinations.

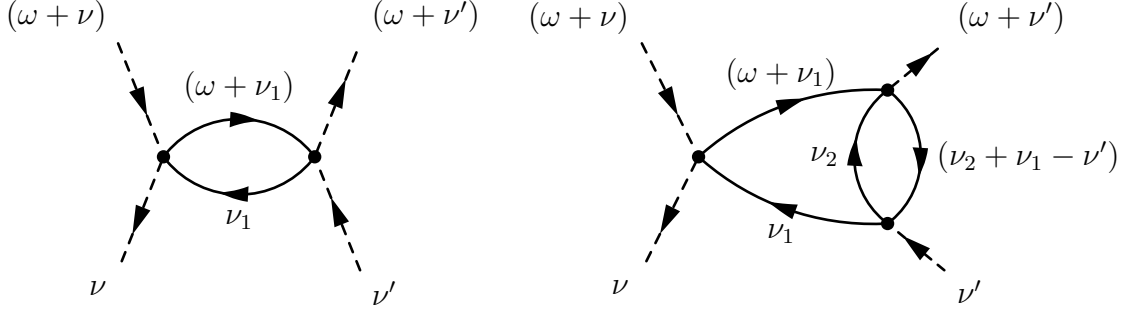


Figure 2.9: Lowest order diagrams contributing to the asymptotics of the particle-hole reducible vertex. Since ν_1 and ν_2 are summed over, they depend only on one external bosonic frequency (left) or one bosonic and one fermionic frequency (right).

One could only calculate two and recover the remaining two through combination and change of frequency notation. However, this change of notation would further limit the available frequency range and thus all four quantities are explicitly calculated.

2.3.1 Vertex asymptotics

Unlike the two-particle Green's function, the vertices F , Γ and Φ do not decay for all high frequencies ν , ν' and ω . This is due to diagrams like the ones shown in Fig. 2.9: whenever two external lines meet at an interaction U , energy conservation immediately eliminates one frequency dependence, resulting in diagrams that do not decay with all three frequencies. This leads to the characteristic shape of the vertex asymptotics as shown for Φ in Fig. 2.10. For a fixed ω , diagrams as the one on the left of Fig. 2.9 contribute to a constant background while the ones on the right create the cross structure. This additional knowledge allows for a cheaper calculation of the full vertex F on larger box sizes through equal-time Green's functions [32]. The vertex asymptotics were applied as follows: The Kernel-functions [33], which encapsulate the asymptotics in each channel, were calculated through equal-times Green's functions along with the susceptibility χ using `w2dynamics`. The Kernel-functions were applied to the full vertex F before inverting the Bethe-Salpeter equation, hoping to mitigate the effect of a finite frequency range and to reduce noise. In one attempt, they were applied again directly to the irreducible vertices Γ . Fig. 2.11 compares the results.

As all of the diagrams in the Kernel-functions are reducible, they do not contribute to the fully irreducible vertex Λ . Therefore, unlike for the irreducible vertices Γ , no significant improvement in cost or quality of the calculation of Λ was found when including the Kernel-functions. A more thorough discussion of this method can be found in [32, 33, 34].

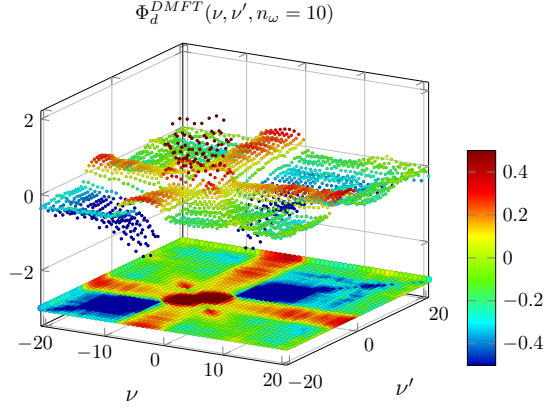


Figure 2.10: Reducible vertex Φ_d from DMFT at $\beta t = 8, U = 4t$ and bosonic frequency $n_\omega = 10$.

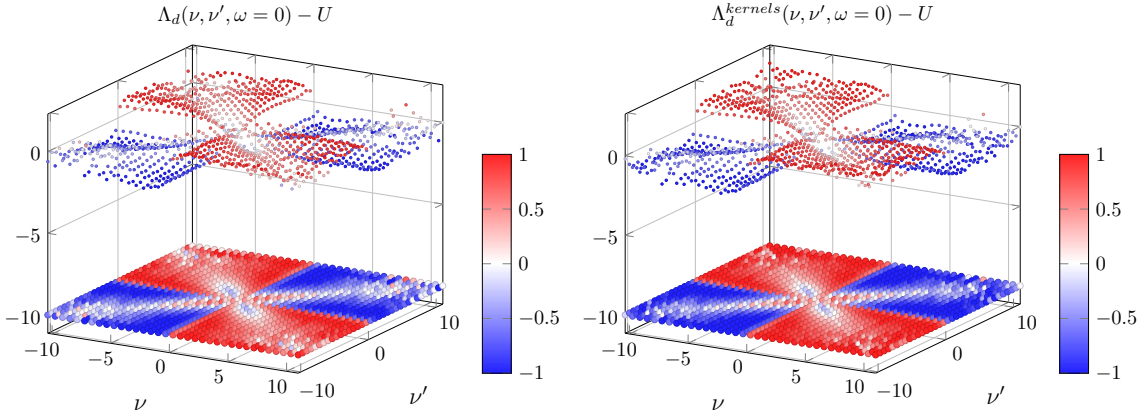


Figure 2.11: The fully irreducible vertex from DMFT in the density channel for $\beta t = 10, U = 3.946t$. On the right, the Kernel-functions were used to improve the asymptotics of the local susceptibility. While a more aggressive application of the Kernel-functions is possible, the crucial low-frequency behavior of Λ could not be improved in a significant way. In this case, the generalized susceptibility was calculated on a $40 \times 40 \times 41$ frequency-box (fermionic \times fermionic \times bosonic) and, for the calculation of $\Lambda_d^{kernels}$, the Kernel-functions were applied to enhance the box-size of the generalized susceptibility to $100 \times 100 \times 101$ to mitigate finite-size effects. Furthermore, they were applied to the generalized susceptibility within the original box where $(\frac{\beta}{\pi})^4 |\nu_1 \nu_2 \nu_3 \nu_4| > 10^4 (1 + \delta_{\nu_1 \nu_2} + \delta_{\nu_1 \nu_4} - \delta_{\nu_1 \nu_2} \delta_{\nu_1 \nu_4})^4$ to cover noise, as discussed in detail in Ref. [34].

2.3.2 Λ , analytically

The fully irreducible vertex can be well approximated analytically in two limits: First, for weak interactions U , the fully irreducible vertex is well approximated by a perturbative expansion. The lowest order diagram, besides the bare interaction, is already of order U^4 and its contribution to $\Lambda_{\uparrow\uparrow}$ is shown in Fig. 2.12. On the other extreme, for $U \gg t$, the atomic limit can be employed: The Hamiltonian is easily diagonalized and one obtains the two-particle Green's function, and subsequently the vertex F , in a strenuous task from the Lehmann representation. In ph -notation, the result is [35]

$$F_{\uparrow\uparrow}^{\nu\nu'\omega} = \beta \frac{U^2}{4} \frac{\delta_{\nu\nu'} - \delta_{\omega 0}}{\nu^2(\nu' + \omega)^2} \left(\nu^2 + \frac{U^2}{4} \right) \left((\nu' + \omega)^2 + \frac{U^2}{4} \right), \quad (2.39)$$

$$\begin{aligned} F_{\uparrow\downarrow}^{\nu\nu'\omega} = & U - \frac{U^3}{8} \frac{\nu^2 + \nu'^2 + (\nu + \omega)^2 + (\nu' + \omega)^2}{\nu(\nu + \omega)(\nu' + \omega)\nu'} - \beta \frac{3U^5}{16} \frac{1}{\nu(\nu + \omega)(\nu' + \omega)\nu'} \\ & - \beta \frac{U^2}{4} \frac{1}{1 + e^{\frac{\beta U}{2}}} \frac{2\delta_{\nu(-\nu' - \omega)} + \delta_{\omega 0}}{(\nu + \omega)^2(\nu' + \omega)^2} \left((\nu + \omega)^2 + \frac{U^2}{4} \right) \left((\nu' + \omega)^2 + \frac{U^2}{4} \right) \\ & + \beta \frac{U^2}{4} \frac{1}{1 + e^{-\frac{\beta U}{2}}} \frac{2\delta_{\nu\nu'} + \delta_{\omega 0}}{\nu^2(\nu' + \omega)^2} \left(\nu^2 + \frac{U^2}{4} \right) \left((\nu' + \omega)^2 + \frac{U^2}{4} \right), \end{aligned} \quad (2.40)$$

$$G(i\nu) = -\frac{i\nu}{\nu^2 + \frac{U^2}{4}}. \quad (2.41)$$

From there, one can extract the fully irreducible vertex in the usual way [34]. Fig. 2.13 shows a result for both extremes.

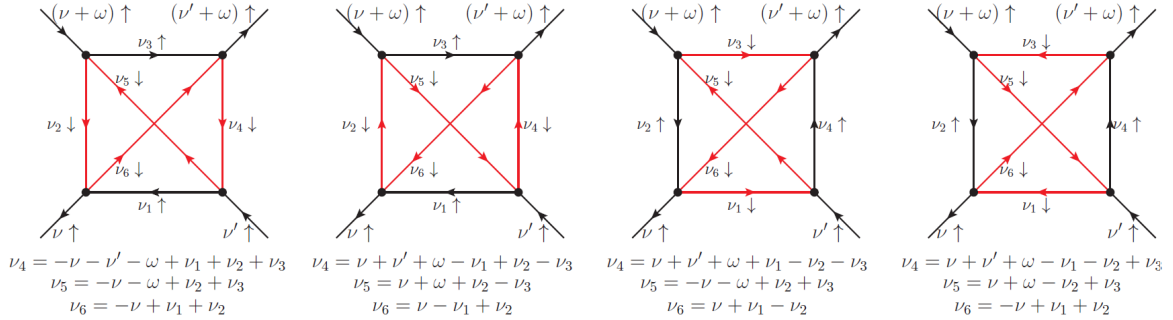


Figure 2.12: Lowest order dynamical contribution to the fully irreducible vertex $\Lambda_{\uparrow\uparrow}$. Taken from Ref. [19].

2.4 Numerical solution of the parquet equations

For the solution of the parquet equations in this work, the `victory`-code was used [26, 36]. This section aims at giving a short overview of the program.

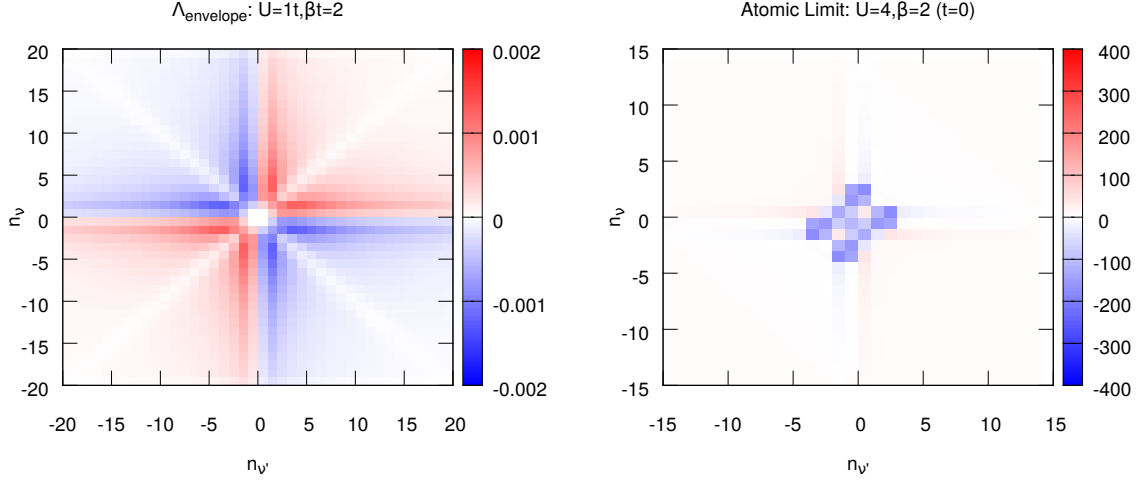


Figure 2.13: (left): Fourth order contribution to Λ_d for $U = 1t, \beta t = 2$ at $\omega = 0$. (right): Λ_d in the atomic limit for $U = 4, \beta = 2$ at $\omega = 0$. Already at this relatively low U/T ratio, Λ is sharply peaked in the atomic limit.

After reading in Λ in the four channels d, m, s, t as introduced in section 2.2.2, the vertices are simply initialized as $F = \Lambda$ and $\Gamma_{ch} = \Lambda$. The self-energy is usually initialized as the Hartree-Fock contribution. A more educated guess, such as the local DMFT self-energy, was not found to reduce the required number of iterations.

The Bethe-Salpeter equations (2.6) are used to calculate the reducible vertex Φ_{ch} in each channel. From Φ_{ch} and Λ , the full vertex F and the irreducible vertices Γ_{ch} are calculated through the parquet equations (2.2). As seen in equations (2.4) and (2.5), the vertices Φ_{ch} have to be known in a larger frequency range than the obtained Γ_{ch} . To prevent the frequency range from shrinking with each iteration, Φ_{ch} is approximated by the Kernel functions that encapsulate the asymptotics of the vertices and already appeared in section 2.3.1. The Kernel functions are themselves approximated by scanning the edges of the available frequency range, see Ref. [33] for further details.

From the full vertex F , the self-energy is updated through the Schwinger-Dyson equation of motion, Eq. (2.31), and the process is repeated with the new self-energy, F and Γ_{ch} until convergence.

For each bosonic frequency and momentum q , the Bethe-Salpeter equations consist of a simple matrix multiplication. For parallelization in the `victory-code`, the vertices for each bosonic q are stored on a separate thread. As the solution of the parquet equations and the Schwinger-Dyson equation still mix bosonic frequencies, they require heavy communication between the threads and thus the communication becomes the

computational bottleneck.

To improve convergence at high interaction and low temperature, a damping parameter for the irreducible vertices is introduced in each iteration of the parquet-solver [37]:

$$\Gamma = \alpha \Gamma_{new} + (1 - \alpha) \Gamma_{old}. \quad (2.42)$$

Since the self-energy is calculated from the vertices through the Schwinger-Dyson equation (2.31), it is also damped according to

$$\Sigma = \alpha \Sigma_{new} + (1 - \alpha) \Sigma_{old}. \quad (2.43)$$

2.4.1 Symmetries

The required memory can be minimized by exploiting the symmetries of the system. The complex conjugation symmetry dictates that $F^{\nu, \nu', \omega} = (F^{-\nu, -\nu', -\omega})^*$. With this knowledge, it suffices to store all the vertices only for positive values of ω and infer the negative ones from the above relation. Implementing this very simple symmetry thus already reduces the required memory by half.

Furthermore, the symmetry of the lattice can be exploited in the **victory-code**. Let S be any operation of the symmetry group of the lattice examined, such as the C_{4v} group for the two-dimensional square lattice. The vertices are only stored for a restricted number of bosonic momenta \mathbf{q}_{IBZ} within what is called the irreducible Brillouin zone, such that each remaining point \mathbf{q} outside the irreducible Brillouin zone is generated by applying a symmetry operation, $\mathbf{q} = S(\mathbf{q}_{IBZ})$. To access the vertex F at \mathbf{q} , the inverse of the symmetry operation in question is applied to all arguments of F :

$$F^{\mathbf{k}, \mathbf{k}', \mathbf{q}} = F^{\mathbf{k}, \mathbf{k}', S(\mathbf{q}_{IBZ})} = F^{S^{-1}(\mathbf{k}), S^{-1}(\mathbf{k}'), \mathbf{q}_{IBZ}}. \quad (2.44)$$

For the two-dimensional square lattice, storing the bosonic momenta only within the irreducible Brillouin zone further reduces the required storage by a factor of eight. The implementation of the lattice symmetry is not included in version 1.0 of the **victory-code** [26]. During this work, version 1.1 was used which exploits the symmetry for the square lattice.

The parquet equations fulfill the crossing symmetry by design [38]. However, one may be tempted to store the full vertex F only in either ph or pp notation and recover the other by a simple transformation of the arguments. Since the vertices are only known on a finite frequency range, some of the values would be unknown, thus breaking the crossing symmetry [26]. For this reason, in the **victory-code** all four vertices $F_{d,m,s,t}$ are stored.

2.4.2 Coarse graining

The maximum \mathbf{k} -resolution achievable in the solution of the parquet equations is severely restricted by the available memory. At several points, such as during the calculation of the self-energy through the Schwinger-Dyson equation, one has to sum products of vertices and one-particle Green's functions over the Brillouin zone. While the self-energy, which in turn is needed to calculate the Green's function, is only known on the \mathbf{k} -resolved points, the dispersion relation of the non-interacting Green's function is usually known analytically and thus at any arbitrary resolution. One can use this fact through coarse graining: at any point \mathbf{k} , we calculate the Green's function as an average around that point, where the averaged terms are calculated from the self-energy at \mathbf{k} and the exact non-interacting Green's function.

$$G(\mathbf{k}) = \frac{1}{N_{cc}} \sum_{\tilde{\mathbf{k}} \in cc} G(\mathbf{k} + \tilde{\mathbf{k}}), \quad (2.45)$$

where $\tilde{\mathbf{k}}$ are points in an area cc centered around \mathbf{k} . N_{cc} is the number of points $\tilde{\mathbf{k}}$ in that area, which is only restricted by computational effort. This method greatly increases the convergence of the parquet equations. In this spirit, one can also interpret DMFT as the most extreme form of coarse graining where the self-energy is only known as an average over the Brillouin zone, yet the local Green's function is calculated with the full dispersion relation [39]. In this case, the parquet equations reproduce the DMFT from the local fully irreducible vertex Λ . Coarse graining is also included in version 1.1 of the victory code, but not in the currently publicly available version 1.0.

2.5 Inverse impurity model

In this step, an impurity model has to be found such that its Green's function equals the local Green's function from D Γ A:

$$G_{AIM}(i\nu) = G_{local}^{D\Gamma A}(i\nu) = \sum_{\mathbf{k}} \frac{1}{i\nu - \epsilon_{\mathbf{k}} - \Sigma_{\mathbf{k}}^{D\Gamma A}(i\nu) + \mu}. \quad (2.46)$$

Once it is found, a new fully irreducible vertex can be calculated for the impurity model with the updated G_{local} . A hint on how this can be achieved is found in the DMFT-cycle (see Sec. 1.3.2): In any iteration n , the local Green's function is calculated from $\Sigma_n(i\nu)$ through

$$G_n^{local}(i\nu) = \sum_{\mathbf{k}} \frac{1}{i\nu - \epsilon_{\mathbf{k}} - \Sigma_n(i\nu) + \mu}. \quad (2.47)$$

From there, the non-interacting Green's function

$$\mathcal{G}_n(i\nu)^{-1} = G_n^{local}(i\nu)^{-1} + \Sigma_n(i\nu) \quad (2.48)$$

serves as the input to calculate the Green's function on the impurity model: $G_n^{imp} = G_n^{imp}[\mathcal{G}_n]$ and the Dyson equation on the impurity is solved for the self-energy of the next iteration

$$\Sigma_{n+1}(i\nu) = \mathcal{G}_n(i\nu)^{-1} - G_n^{imp}(i\nu)^{-1}. \quad (2.49)$$

Inserting Eq. (2.49) into Eq. (2.48) after the shift $n \rightarrow n + 1$ gives

$$\mathcal{G}_{n+1}(i\nu)^{-1} = \mathcal{G}_n(i\nu)^{-1} + G_{n+1}^{local}(i\nu)^{-1} - G_n^{imp}(i\nu)^{-1}. \quad (2.50)$$

Equivalently, this can be expressed through the hybridization function $\Delta(i\nu) = i\nu + \mu - \mathcal{G}(i\nu)^{-1}$ as

$$\Delta_{n+1}(i\nu) = \Delta_n(i\nu) + G_n^{imp}(i\nu)^{-1} - G_{n+1}^{local}(i\nu)^{-1}. \quad (2.51)$$

This scheme can be adapted to find the required impurity model for the fully self consistent parquet D Γ A by replacing G^{local} with $G_{local}^{D\Gamma A}$. Omitting the inversion of both Green's functions has been found to give the same results after a sufficient number of iterations while being numerically more stable, so that the hybridization-update used in this implementation is

$$\Delta_{n+1}(i\nu) = \Delta_n(i\nu) + G_n^{imp}(i\nu) - G_{local}^{D\Gamma A}(i\nu). \quad (2.52)$$

The high-frequency behavior of both Green's functions in Eq. (2.52) is determined by the $\frac{1}{i\nu}$ -term and is thus the same. It is therefore not updated for Δ and should be assumed correctly in Δ_0 . For the Hubbard model with local interaction only and hopping amplitude t , the asymptotic form of the hybridization function is the same as that of Δ_{DMFT} ,

$$\Delta(i\nu) = \frac{z|t|^2}{i\nu} + \mathcal{O}\left(\frac{1}{(i\nu)^2}\right), \quad (2.53)$$

where z is the coordination number. Later we will introduce non-local interactions into the parquet D Γ A for the benzene molecule by adding the resulting non-local Hartree-Fock term to the self-energy, without treating the non-local interactions explicitly in the auxiliary impurity. This changes the high-frequency behavior of the hybridization function significantly. To see how, we again write down the Dyson equation on the impurity:

$$\mathcal{G}(i\nu)^{-1} = i\nu - \Delta(i\nu) + \mu = G_{loc}^{-1}(i\nu) + \Sigma_{imp}(i\nu). \quad (2.54)$$

To find the high frequency behavior of this equation, we expand G_{loc} in terms of $\frac{1}{i\nu}$:

$$\begin{aligned}
G_{loc} &= \frac{1}{i\nu} \frac{1}{N} \sum_k \frac{1}{1 - \frac{\epsilon_k + \Sigma_k - \mu}{i\nu}} \\
&= \frac{1}{i\nu} \left(1 + \frac{1}{N} \sum_k \left[\left(\frac{\epsilon_k + \Sigma_k - \mu}{i\nu} \right) + \frac{(\epsilon_k + \Sigma_k - \mu)^2}{(i\nu)^2} \right] \right) + \mathcal{O} \left(\frac{1}{(i\nu)^3} \right). \quad (2.55)
\end{aligned}$$

Expanding the inverse G_{loc}^{-1} again gives the required term for the Dyson-equation. With $\frac{1}{N} \sum_k \Sigma_k = \Sigma_{loc}$ and $\sum_k \epsilon_k = 0$,

$$G_{loc}^{-1}(i\nu) = i\nu \left(1 - \frac{\Sigma_{loc} - \mu}{i\nu} - \frac{1}{N} \sum_k \frac{(\epsilon_k + \Sigma_k - \mu)^2}{(i\nu)^2} + \left(\frac{\Sigma_{loc} - \mu}{i\nu} \right)^2 + \mathcal{O} \left(\frac{1}{(i\nu)^3} \right) \right) \quad (2.56)$$

At half filling, the Hartree term of Σ_{loc} is exactly compensated by the chemical potential $\mu = \Sigma_{Hartree}$, so that $\Sigma_{loc} - \mu = \mathcal{O}(\frac{1}{i\nu})$. Hence the last term in the parentheses is of order $\mathcal{O}(\frac{1}{(i\nu)^4})$ and can be neglected. Furthermore, we make use of $G_{loc} = G_{imp}$ and $\Sigma_{loc} - \Sigma_{imp} = \mathcal{O}(\frac{1}{(i\nu)^2})$. Inserting this into Eq. (2.54) gives the desired asymptotic expression for the hybridization function,

$$\Delta(i\nu) = \frac{1}{i\nu} \left(\frac{1}{N} \sum_k (\epsilon_k + \Sigma_k(i\nu) - \mu)^2 \right) + \mathcal{O} \left(\frac{1}{(i\nu)^2} \right). \quad (2.57)$$

2.5.1 Uniqueness of the solution

The Matsubara frequencies are proportional to $\frac{1}{\beta} = T$. For high temperatures, both the Green's function and the hybridization are thus dominated by the $\frac{1}{i\nu}$ behavior except for very few Matsubara frequencies around zero. One can then parametrize the hybridization function easily with only a few variables, for example through a decomposition in Legendre-polynomials in τ [40]. At half-filling, we know that due to particle-hole symmetry they should be symmetric around $\frac{\beta}{2}$, thus eliminating all odd Legendre coefficients. The known value at $\tau = 0$ puts a further constraint on the coefficients. To see how the number of relevant Legendre-coefficients changes with temperature, Fig. 2.14 compares their magnitude for DMFT-solutions at various temperatures.

At $\beta t = 2$, only the first three coefficients contribute significantly, one of them being determined through $\Delta(\tau = 0)$. To investigate the uniqueness of the solution of the inverse impurity problem, that is finding a hybridization function such that the impurity model gives a specific Green's function, one can then scan the two-dimensional parameter space. Fig. 2.15 gives a map of the solutions of impurity models with different hybridization functions. The hybridization functions and the resulting identical Green's functions of the points marked as 1 and 2 are shown in Fig. 2.16. There are thus two solutions to finding an impurity model with that Green's function.

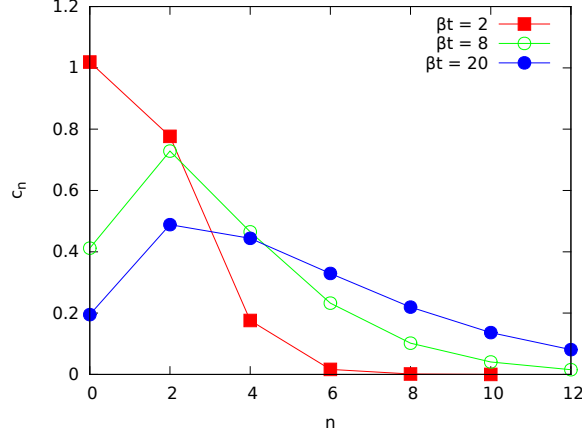


Figure 2.14: Legendre coefficients of DMFT-hybridization functions for various temperatures at $U = 4t$. The uneven coefficients are zero due to particle hole symmetry at half filling. At $\beta t = 2$, already the sixth coefficient is negligibly small, enabling the parametrization in the rest of this section.

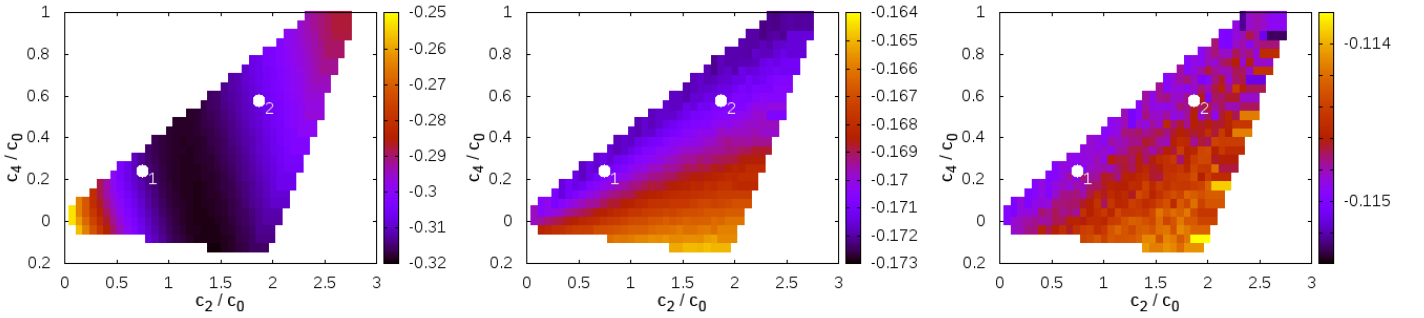


Figure 2.15: Map of hybridization functions and their resulting G^{AIM} at $\beta t = 2, U = 4t$ and half filling. The colorbar gives the imaginary part of the Green's function at the first (left), second (middle) and third (right) Matsubara frequency. The hybridization functions are composed of only the first three even Legendre polynomials and normalized to give the correct asymptotics for the 2D-square Hubbard model. The x - and y -axes denote the second and fourth Legendre coefficient of the hybridization function, divided by the zeroth coefficient. Only strictly positive and convex hybridization functions were taken into account, hence the borders of the triangle shape. For larger Matsubara frequencies, the Green's function is already dominated by the $\frac{1}{i\nu}$ behavior at this temperature. The point marked as 1 and 2 give the same Green's function, as demonstrated in Fig. 2.16, and Δ_1 is close to Δ_{DMFT} .

Although the one-particle Green's function is identical for the two baths, the self-energy and the fully irreducible vertex generated from Δ_2 are vastly different, as seen in Fig. 2.17. The fully irreducible vertex from Δ_2 almost diverges and does not allow to further converge the parquet equations. Hence one has to be careful to pick a good initial

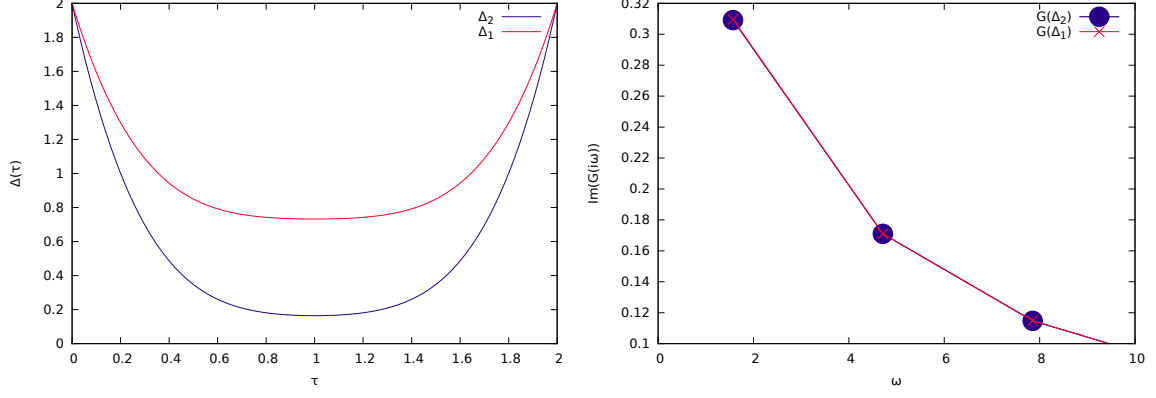


Figure 2.16: Left: The hybridization functions for the two points marked in Fig. 2.15. Right: The resulting Green's function. Although the hybridizations differ greatly, the resulting Green's functions are practically indistinguishable.

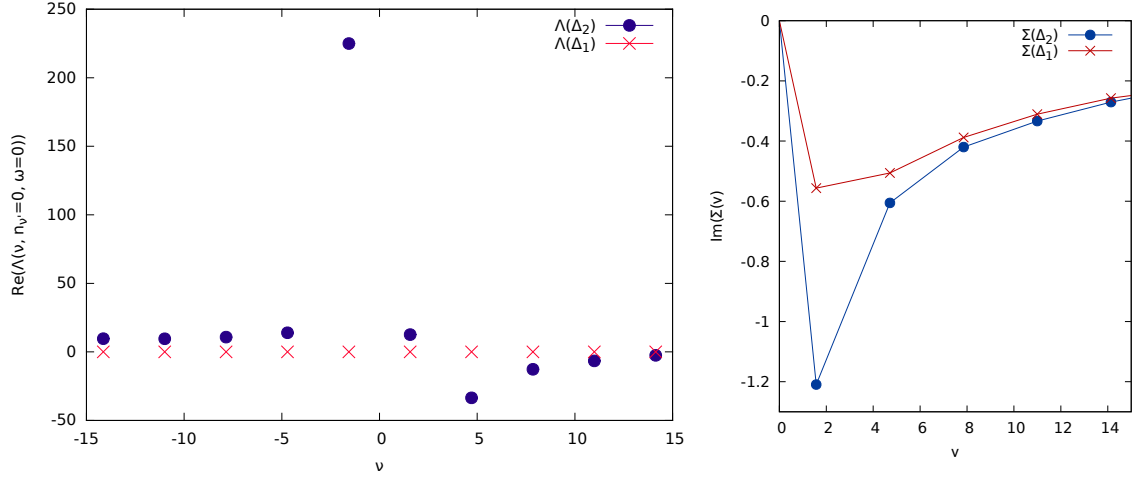


Figure 2.17: The fully irreducible vertex at $n_v = 0, \omega = 0$ (left) and the self-energy (right) for the two hybridization functions from Fig. 2.16.

hybridization in order to get a physical fully irreducible vertex. Both Δ_{DMFT} and a hybridization calculated from the local part of Σ^{DGA} were found to work well. At lower temperatures and a finer resolution in Matsubara frequencies, both the possible hybridization function as well as the requirements on the resulting Green's function become more nuanced at an equal rate. The assumption that also at lower temperatures there would only be one solution that gives a physical Λ was corroborated by converging from different starting hybridization functions.

2.6 Similar methods

A computationally less demanding version of D Γ A, namely the ladder D Γ A, can be applied when there is one dominating channel [41]. For example, in a system with magnetic ordering, the particle-hole channel will dominate and one can restrict the particle-particle-reducible vertex to its local part, eliminating the repeated solution of the parquet equations and thus the most expensive step from the computation. Furthermore, the Green's function is approximated by the (non-local) $G_{DMFT}(\nu, \mathbf{k})$, so the ladder D Γ A consists in a one-shot generation of the so-called ladders in one channel through the Bethe-Salpeter equation and subsequent calculation of the self-energy through the Schwinger-Dyson equation.

Another simplification of the parquet D Γ A is the parquet approximation, where Λ is approximated by the bare interaction U . It can thus also be executed using the `victory-code`.

Some results of both of these methods will be compared to the parquet D Γ A in Sec. 3.2.2.

Chapter 3

Results

3.1 Benzene

In this section, DfA results for the benzene molecule are compared to exact diagonalization. Due to the simplicity of the benzene molecule, a semi-empirical model is available that fits very well to experimental data, called the Pariser-Parr-Pople model [42]. Just like the one-dimensional Hubbard model it contains hopping and the local interaction, but it further includes non-local interaction between electrons on different sites. Its Hamiltonian is

$$H_{PPP} = - \sum_{\sigma} \sum_{i=1}^6 t(\hat{c}_{i+1\sigma}^{\dagger} \hat{c}_{i\sigma} + h.c.) + U \sum_{i=1}^6 \hat{n}_{i\uparrow} \hat{n}_{i\downarrow} + \frac{1}{2} \sum_{i \neq j} V_{ij} (\hat{n}_{i\uparrow} + \hat{n}_{i\downarrow})(\hat{n}_{j\uparrow} + \hat{n}_{j\downarrow}) \quad (3.1)$$

The parameters are adjusted to account for screening and fit the experimental results. They are given in Table 3.1.

The same parameters were applied to DfA so the exact diagonalization results could be taken as a benchmark for the method, even though the model, being one-dimensional and including non-local interactions, is almost a worst case scenario for DfA. The non-local interactions were not included in the DMFT calculation that serves as a starting point

	t	U	V_1	V_2	V_3
eV	2.539	10.06	7.19	5.11	4.58
units of t	1	3.963	2.833	2.014	1.804

Table 3.1: Parameters of the Pariser-Parr-Pople model. V_1 is the nearest neighbor interaction, V_2 the next-nearest neighbor interaction and V_3 the next-next-nearest neighbor interaction.

for D Γ A, but only through the non-local Hartree-Fock term in the solution of the parquet equations [43]:

$$\Sigma_{\uparrow}^{HF}(\nu; k) = \sum_{\omega; q} \overbrace{G_{\uparrow}(\nu - \omega; k - q)}^{U(q)} = \sum_q \hat{n}_{\uparrow(k-q)} U(q)$$

The introduction of these static but k-dependent parts of the self-energy also changes the required asymptotics of the hybridization function, as discussed in Sec. 2.5. The parquet equations for the PPP model were subsequently solved with an extended version of the `victory-code` that includes non-local interaction [44].

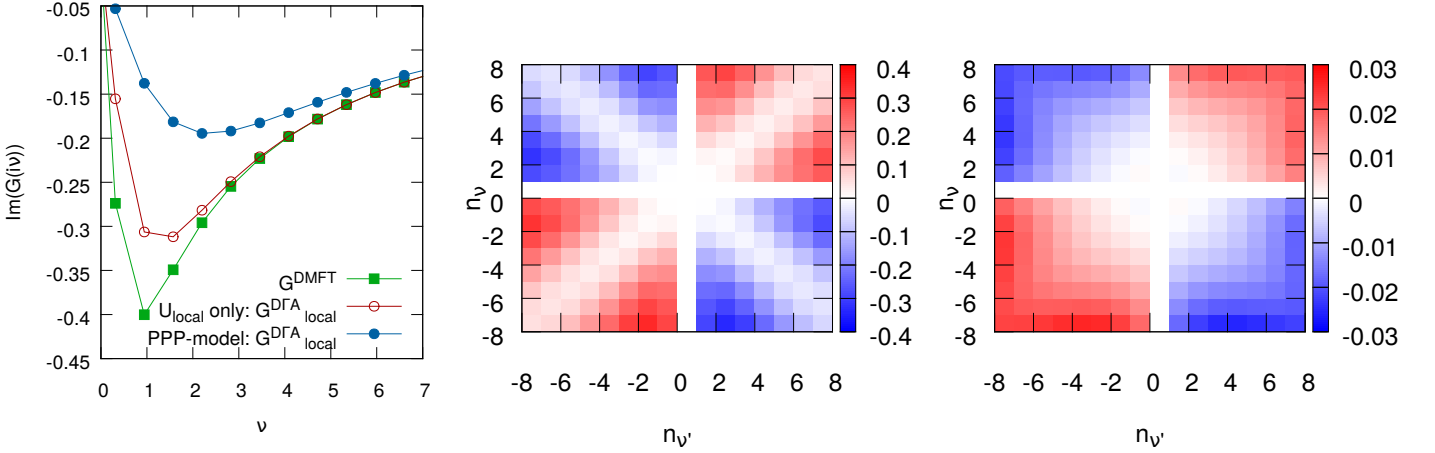


Figure 3.1: Left: Local Green's function from DMFT and D Γ A with local interaction only and the PPP-model parameters. Middle: Lowest order dynamic contribution to $\Lambda_{\uparrow\uparrow}(\nu, \nu', \omega = 0)$ in ph -notation (corresponding to Fig. 2.12), calculated from the DMFT Green's function. Right: Same contribution calculated from the local D Γ A Green's function for the PPP-model. Note the different scale between the two plots.

Just like for the 2D-Hubbard model, the parquet D Γ A calculation begins with a solution from DMFT which does not take the non-local interaction into account at all. Only after one iteration of D Γ A, the hybridization of the impurity is updated to match the new local Green's function which now also contains an approximation of the non-local interaction. The outer-self consistency in D Γ A is therefore especially important in this case since the initial guess for Λ from DMFT is particularly inaccurate. Specifically, the introduction of V_{ij} notably reduces the magnitude of the local Green's function at low frequencies, as seen in the leftmost plot of Fig. 3.1. Physically, this means that the

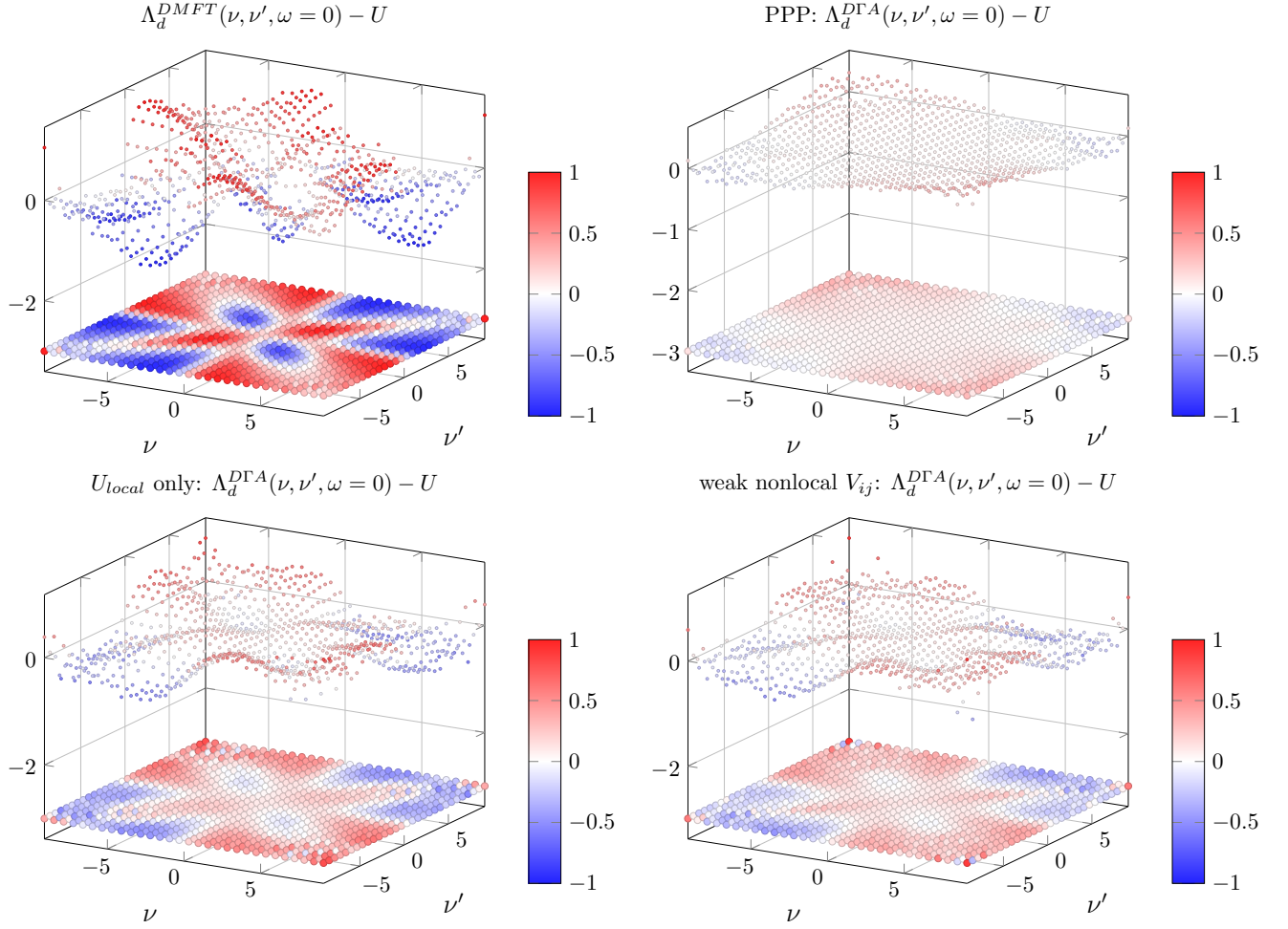


Figure 3.2: The fully irreducible vertex Λ for $\beta t = 10$, $U = 3.963t$. Top left: DMFT only. Bottom left: fully self-consistent parquet D Γ A with local interaction only. Bottom right: fully self-consistent parquet D Γ A with $V_1 = 0.5t$, $V_2 = 0.2t$, $V_3 = 0.1t$. Top right: fully self-consistent parquet D Γ A with the parameters from table 3.1.

system is more metallic. The low-frequency behavior of the Green's function is crucial for the generation of the dynamic part of the fully irreducible vertex Λ as the higher order diagrams are basically sums of products of Green's functions which have their maximum at a low frequency. Fig. 3.1 compares the lowest-order contribution to Λ , the envelope diagram from Fig. 2.3.2, calculated once from the DMFT-Green's function and once from $G_{\text{local}}^{D\Gamma A}$ with non-local interactions of the PPP-model.

The same happens for higher order diagrams, so all dynamic contributions to Λ almost vanish and only the bare interaction U survives. Fig. 3.2 shows the results for Λ as calculated from the auxiliary impurity for DMFT and D Γ A with three different strengths of V_{ij} . Already for $V_{ij} = 0$, DMFT overestimates the dynamic contributions to Λ . The introduction of nonlocal interaction reduces them further, and for the Pariser-Parr-Pople model $\Lambda \approx U$.

With the dynamic parts of Λ suppressed, the fully self-consistent parquet D Γ A closely resembles the parquet approximation, where Λ is approximated by the bare interaction. Fig. 3.3 compares results for the self-energy from exact diagonalization to one-shot D Γ A, self-consistent D Γ A and the parquet approximation. As expected, the parquet approximation and the fully self-consistent parquet D Γ A are very similar. Both show much more accurate results than the one-shot D Γ A when compared to the exact diagonalization data, confirming the importance of the outer self-consistency in this case.

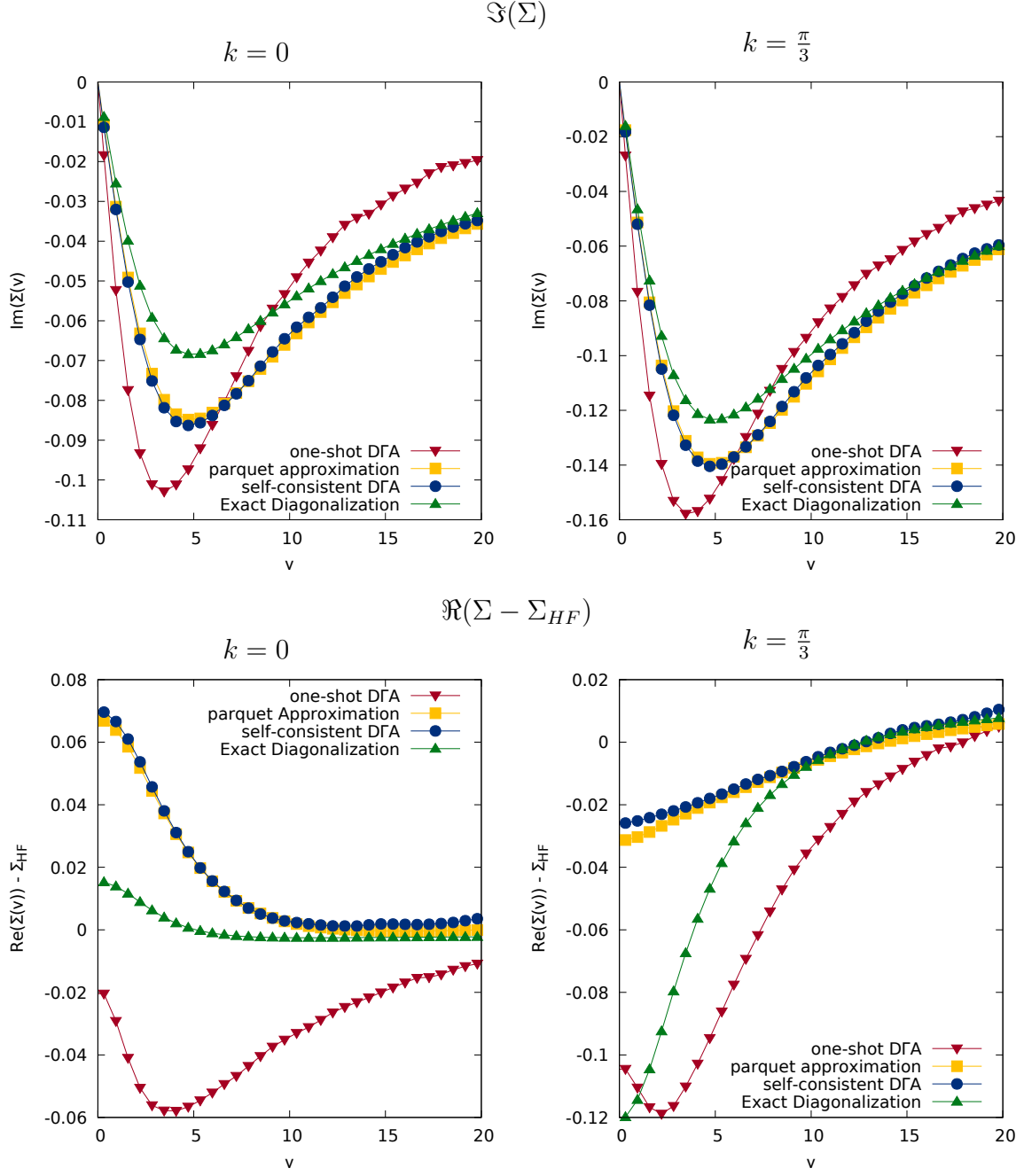


Figure 3.3: Self energy calculated from one-shot D Γ A, parquet approximation, self-consistent D Γ A and exact diagonalization with the parameters from Table 3.1 and $\beta t = 10$. Top: Imaginary part for $k = 0$ (left) and $k = \frac{\pi}{3}$ (right). Bottom: Real part without Hartree-Fock contribution again for $k = 0$ (left) and $k = \frac{\pi}{3}$ (right). The DMFT self-energy is not shown here because it is much larger in magnitude, as its maximum is $|\Im(\Sigma_{DMFT})|^{max} \sim 0.55$.

3.2 2D-Hubbard model

During the parquet D Γ A cycle, various quantities are computed that help to interpret the properties of the system in question. First of all, there are the one-particle properties such as the non-local self-energy $\Sigma^{D\Gamma A}(\mathbf{k}, \nu)$ and thus, in combination with the dispersion relation and the chemical potential, the interacting Green's function and the shape of the Fermi-surface. These are complemented by the two-particle vertices, which give insight into phenomena such as magnetic ordering and possibly superconductivity.

3.2.1 Magnetic and superconducting order

When looking for possible instabilities and ordering symmetries, looking directly at the vertices is sometimes impractical. Instead, in the following we introduce eigenvalues, eigenvectors and effective interactions, which give a much more compact representation of the results.

3.2.1.1 Eigenproblem

The `victory-code` produces the eigenvalues and eigenfunctions of the Bethe-Salpeter equations. In the *pp*-channel, they are most interesting at $\mathbf{q} = 0, \omega = 0$ and capture possible pairing between wave vectors \mathbf{k} and $-\mathbf{k}$. The corresponding eigenequation reads

$$\lambda_\alpha \Phi_\alpha(k) = \frac{1}{\beta} \sum_{k'} \Gamma_{pp}(k, k') G(k') G(-k') \Phi_\alpha(k'), \quad (3.2)$$

where the momentum indices are given in particle-particle notation (see Sec. 1.2.2.1). When the largest eigenvalue λ in the particle-particle channel gets close to one, the susceptibility diverges signaling the superconducting instability. At that point, the Bethe-Salpeter equations becomes equivalent to the gap equation and the eigenfunction becomes equivalent to the order parameter Δ_k [45]. Furthermore, the q -resolved eigenvalues $\mu_{q,\alpha}$ in the magnetic channel (in particle-hole notation) give an overview of the possible magnetic ordering in the system.

$$\mu_{q,\alpha} \Psi_{q,\alpha}(k) = \frac{1}{\beta} \sum_{k'} \Gamma_m(k, k') G(k' + q) G(k') \Psi_{q,\alpha}(k') \quad (3.3)$$

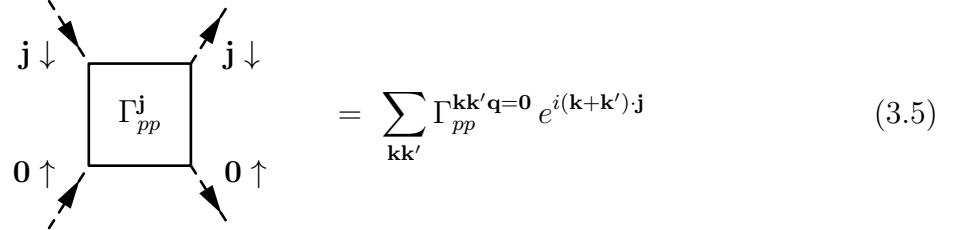
Again, an eigenvalue of one leads to a divergence in the susceptibility at that momentum transfer and for antiferromagnetic ordering the largest eigenvalue is at $\mathbf{q} = (\pi, \pi)$.

3.2.1.2 Pairing interaction

Looking at the Bethe-Salpeter equation in the particle-particle channel, we can interpret the irreducible vertex in that channel as an effective pairing interaction [46]. Since the pair is expected to have wave numbers \mathbf{k} and $-\mathbf{k}$, we evaluate Γ_{pp} at $\mathbf{q} = (0, 0)$. Furthermore, the required spin-combination $\overline{\uparrow\downarrow}$ of the pairing interaction is obtained from the singlet- and triplet-channel through

$$\Gamma_{pp, \overline{\uparrow\downarrow}} = \Gamma_{pp, \uparrow\downarrow} - \Gamma_{pp, \uparrow\uparrow} = \frac{1}{2}(\Gamma_t - \Gamma_s) := \Gamma_{pp}. \quad (3.4)$$

It will be simply referred to as Γ_{pp} in the following. The pairing interaction between site $\mathbf{0}$ and site \mathbf{j} is obtained through a Fourier transform:



$$= \sum_{\mathbf{k}, \mathbf{k}'} \Gamma_{pp}^{\mathbf{k}, \mathbf{k}', \mathbf{q}=0} e^{i(\mathbf{k}+\mathbf{k}') \cdot \mathbf{j}} \quad (3.5)$$

In order for superconductive pairing to be energetically favorable, the pairing interaction should be attractive in analogy to the attractive electron-electron potential mediated by phonons in conventional superconductivity. Indeed, an attractive interaction between neighboring sites was found in the parquet DΓA and the parquet approximation and will be shown for several parameter sets in Sec. 3.2.1.4. This attractive interaction was also found by Bulut [45] in QMC calculations.

3.2.1.3 Momentum dependent susceptibility

The transfer-momentum dependent form of the magnetic susceptibility contains information about the magnetic ordering of the system. As stated above, at low temperatures and near half filling it has a sharp peak at $\mathbf{q} = (\pi, \pi)$. With doping, the maximum moves away from (π, π) . To compare the results of DΓA with those of another method, where a larger lattice is achievable, we follow Ref. [47]. Herein, we calculate $\chi_m^{DMFT}(\mathbf{q}, \omega = 0)$ from the irreducible vertex Γ_m^{DMFT} and the k -summed bare susceptibility $\chi_{0,ph}^{DMFT}(\mathbf{q}, \omega = 0)$ through the Bethe Salpeter equation. This method violates the Mermin-Wagner theorem [48], in that the magnetic susceptibility diverges at (π, π) at low but non-zero temperatures and the above calculation fails. To compare it to $\chi_m^{D\Gamma A}(\mathbf{q}, \omega = 0)$, calculations at a temperature of $\beta t = 4$, above the DMFT Néel temperature, were done. Fig. 3.4 shows the evolution of the maximum of $\chi_m(\mathbf{q})$ with doping.

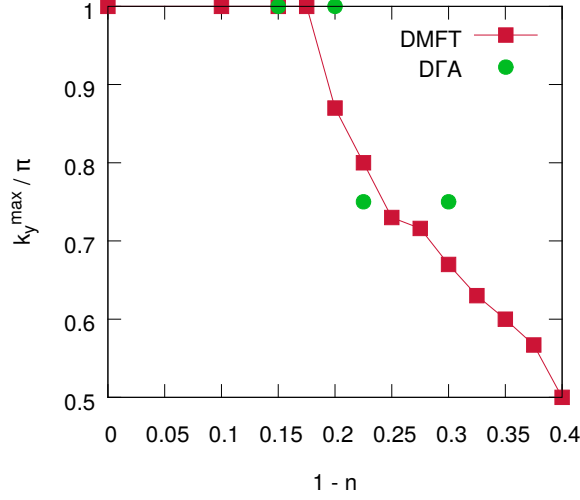


Figure 3.4: Position of the maximum of $\chi_m(\mathbf{q})$ is at (π, k_y^{\max}) (and the symmetrically identical points). Even for the limited \mathbf{k} -resolution due to the system size of 8×8 in (one-shot) DGA, the position of the maximum clearly resembles that of DMFT. $\beta t = 4, U = 4t$.

The peak in the magnetic susceptibility is closely connected to the symmetry of the superconducting order parameter through the effective interaction, as discussed in Sec. 1.1. This can also be seen from the parquet equations, specifically Eq. (2.5), after some rearranging:

$$\Gamma_{pp}^{kk'q} = \Lambda_{pp}^{kk'q} + \Phi_m^{kk'(q-k-k')} + \frac{1}{2}\Phi_m^{k(q-k')(k'-k)} - \frac{1}{2}\Phi_d^{k(q-k')(k'-k)} \quad (3.6)$$

The pp -subscript without spin indices is defined as in Eq. (3.5). Close to magnetic ordering, the Φ_m -terms will dominate the right hand side of this equation, as well as the full vertex in the connected part of the magnetic susceptibility. Setting the bosonic momentum and frequency to zero, we thus see that the effective interaction $\Gamma^{kk'q=0}$ is proportional to the magnetic susceptibility with transfer momentum $\mathbf{q} = \mathbf{k} - \mathbf{k}'$.

3.2.1.4 Symmetry of the eigenfunctions

Fig. 3.5 shows the pairing interaction and the corresponding eigenfunctions from the self-consistent parquet DGA on a 6×6 cluster at three different fillings. In all cases, for the small cluster size considered there is a strong interaction with the most distant site within that cell. At half filling, it is strongly repulsive while there is an attraction between nearest neighbors with opposing spins. This attraction leads to the $d_{x^2-y^2}$ pairing, which already manifests itself in the symmetry of the eigenfunction at eigenvalues $\lambda \ll 1$ far from the superconducting instability. Away from half filling, the interaction with the most distant site becomes attractive at $n \simeq 0.7$, causing the eigenfunction of the largest eigenvalue to reflect the pairing with that site in real space. In \mathbf{k} -space, this leads to

an unusual s-wave symmetry, further referred to as \tilde{s} . Fig. 3.8 shows the evolution of the largest eigenvalue with $d_{x^2-y^2}$ and s or \tilde{s} symmetry over various fillings. The $d_{x^2-y^2}$ -pairing has a maximum at half filling, unlike the physical situation in cuprates where the superconducting dome is centered around $n \simeq 1 - \frac{1}{8}$. The same result was found in Ref. [49] for DCA-calculations at interaction $U \lesssim 6t$. At larger U , they found the pairing to be suppressed at half filling, along with the emergence of a pseudogap [50, 51]. Also, the introduction of next-nearest neighbor hopping t' was found to break the symmetry between electron- and hole-doping. For the parquet DGA, however, no pseudogap was found yet because the interaction strength and temperature are limited by the divergence of the parquet equations.

The origin of the attraction to the furthest site at $n = 0.7$ and thus the strange \tilde{s} symmetry is currently not completely understood and cluster-size dependent. Fig. 3.6 shows the effect to be significantly weaker on a larger cluster size of 8×8 when compared to the 6×6 cluster with $n = 0.7$ shown in Fig. 3.5. Also with the larger system size, the eigenvalue of the strange symmetry \tilde{s} is significantly smaller and close to the eigenvalues with other symmetries. However, this may be due to a shift in the maximum of the \tilde{s} -eigenvalue away from $n = 0.7$, as indicated by results from the parquet approximation [52]. To reach a conclusive explanation of the strange behavior of the pairing interaction and the eigenfunctions, calculations on even larger clusters may be necessary. The \tilde{s} -symmetry fades with even heavier doping and gives way to the usual s -symmetry, as shown in Fig. 3.7 for the parquet approximation at $n = 0.65$. Note however, that above some doping level there will no longer be any superconducting symmetry breaking.

Besides the symmetries mentioned above, also eigenfunctions resembling the stripe-order [53] (p-wave) were found, although never at the dominating eigenvalue. Fig. 3.9 shows one example.

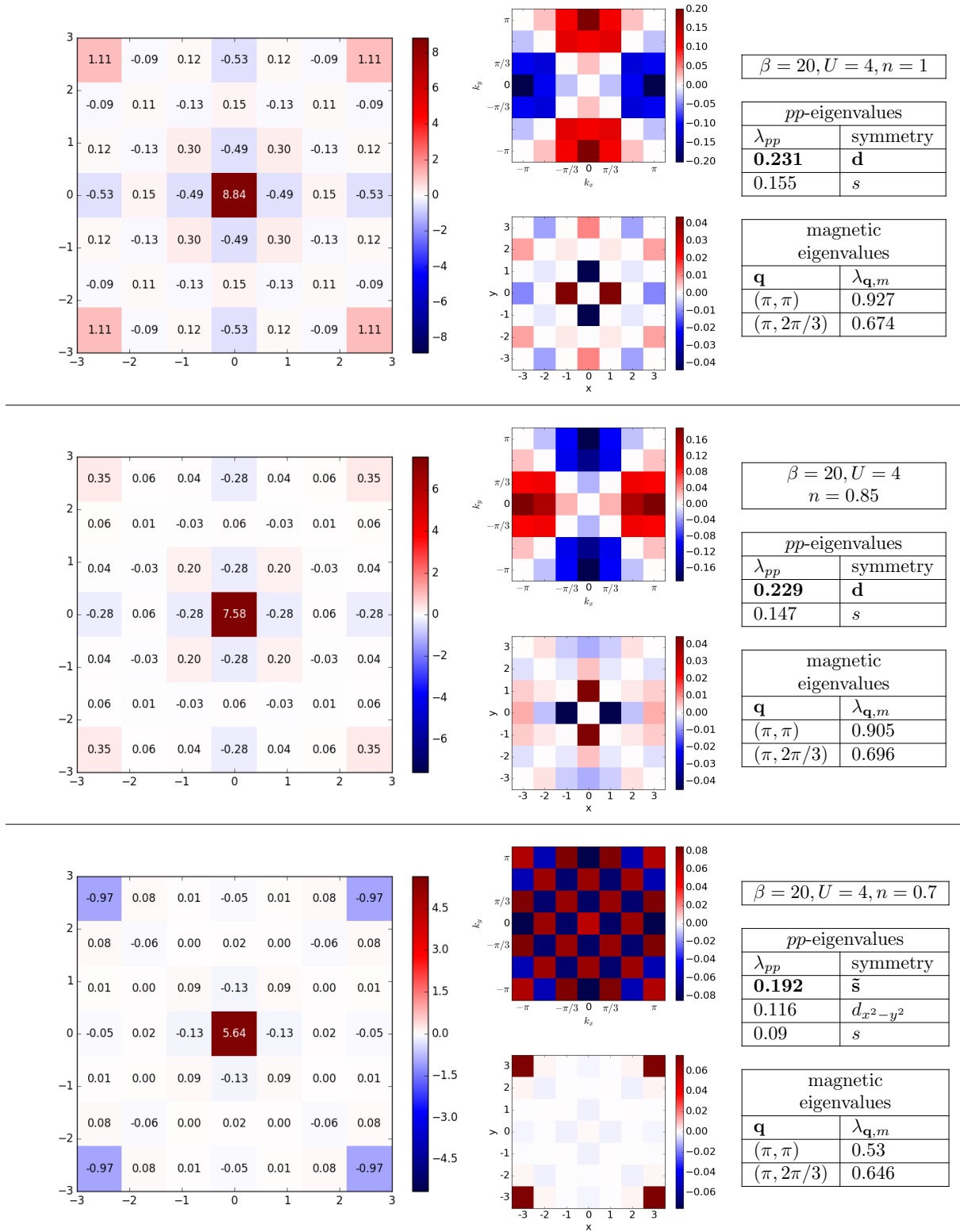


Figure 3.5: Left: Pairing interaction in real space, as described in Sec. 3.2.1.2. Middle: eigenfunction of the leading eigenvalue of the pp-Bethe-Salpeter equation in \mathbf{k} -space and real space. Right: Parameters, leading eigenvalues in the pp-channel with their respective symmetry and largest eigenvalue in the magnetic channel for $\mathbf{q} = (\pi, \pi)$, which is close to one for antiferromagnetic ordering, and for $\mathbf{q} = (\pi, 2\pi/3)$, where the magnetic susceptibility peaks for lower fillings at the used cluster size of 6×6 .

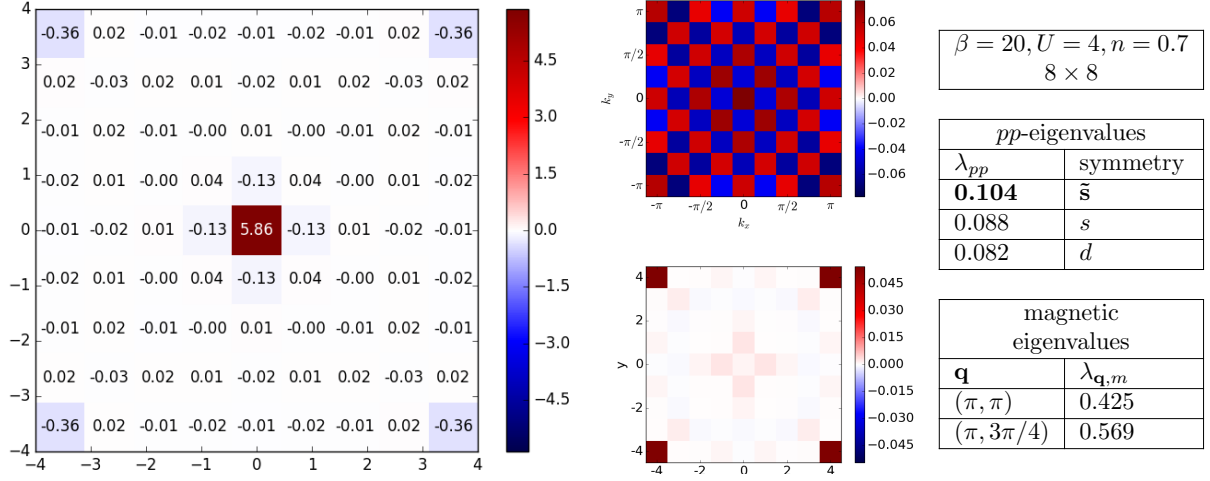


Figure 3.6: As Fig. 3.5, but for $\beta t = 20, U = 4t, n = 0.7$ on an 8×8 cluster.

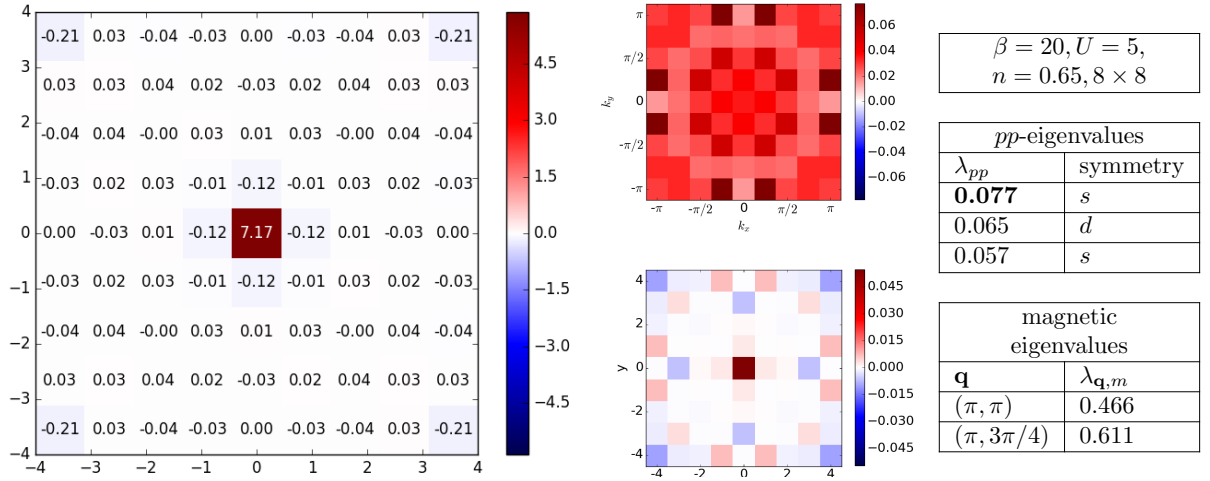


Figure 3.7: As Fig. 3.5, but for $\beta t = 20, U = 5t, n = 0.65$ on an 8×8 cluster from the parquet approximation.

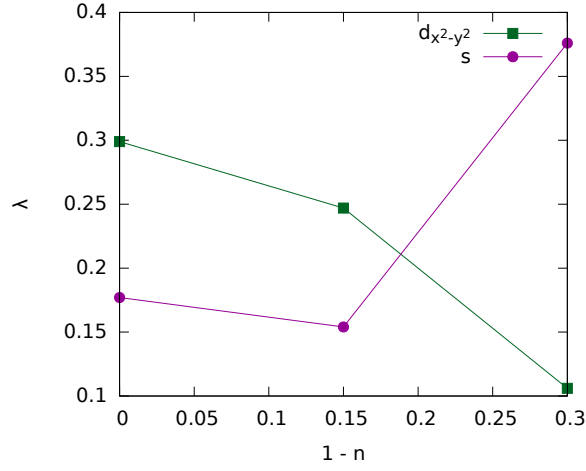


Figure 3.8: Largest eigenvalues of the pp -Bethe-Salpeter equation at $\beta t = 20$, $U = 4t$ for various fillings on a 6×6 cluster. Note that the point at $n = 0.7$ has the unusual \tilde{s} -symmetry mentioned above.

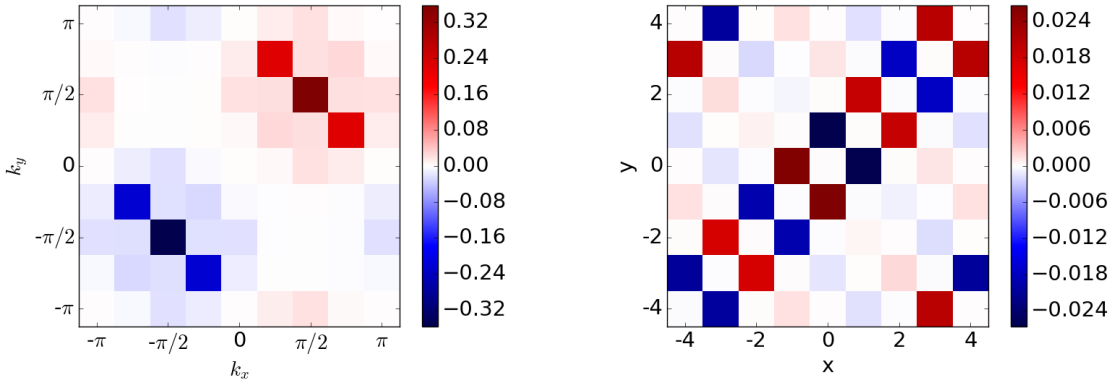


Figure 3.9: Eigenvector showing a p -wave symmetry in \mathbf{k} -space (left) and stripe-like order in real space (right) at $\beta t = 20$, $U = 4t$, $n = 1$ on an 8×8 cluster. The corresponding eigenvalue is 0.147, compared to the largest eigenvalue in the pp -channel, 0.344, which has $d_{x^2-y^2}$ -symmetry.

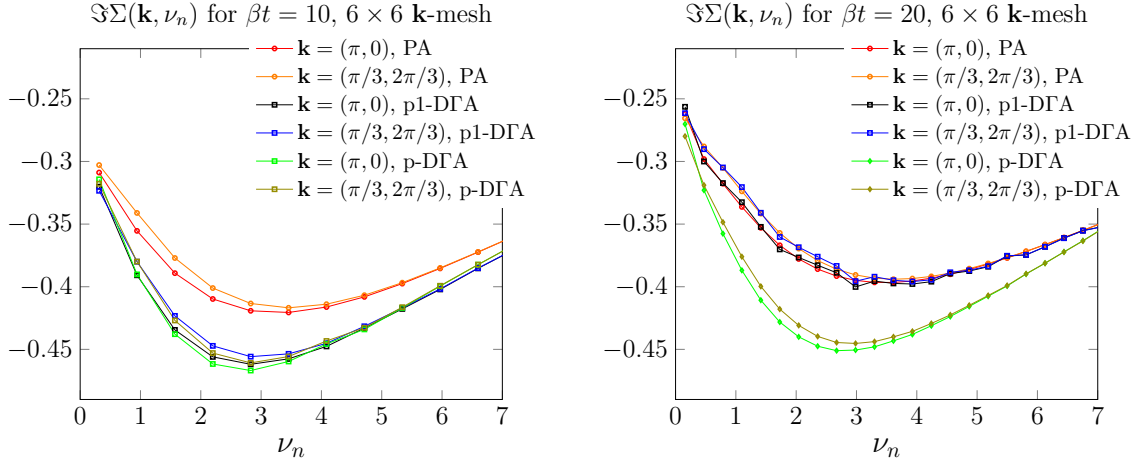


Figure 3.10: Imaginary part of the self-energy near the fermi-surface from self-consistent parquet DΓA (p-DΓA), one-shot parquet DΓA (p1-DΓA) and parquet approximation (PA [52]) at $U = 4t$ and half filling.

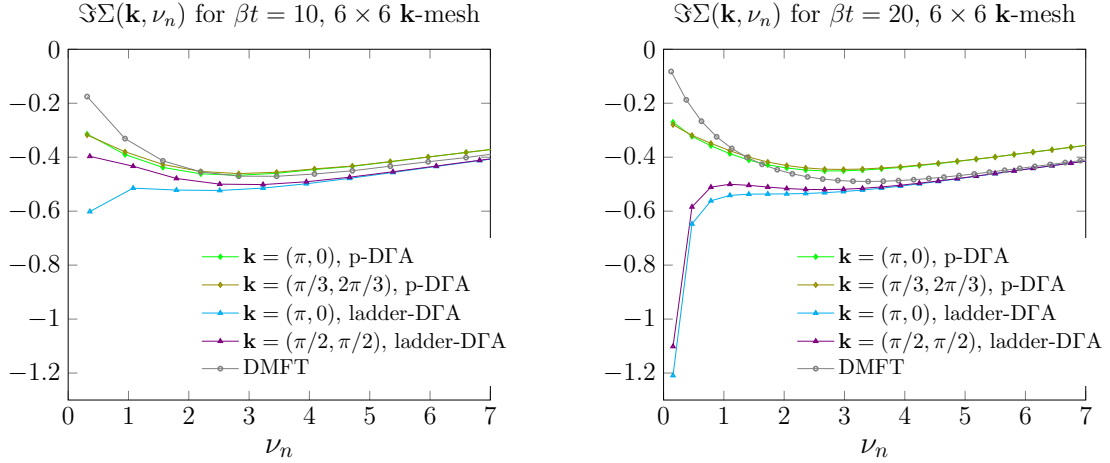
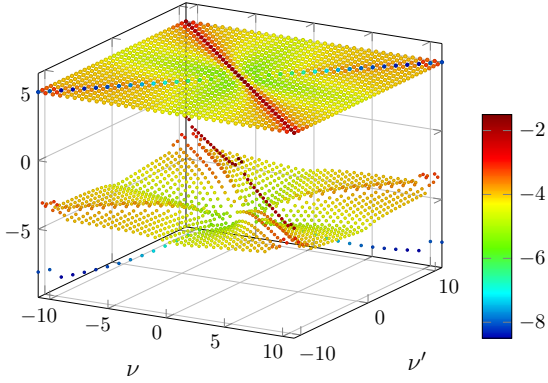


Figure 3.11: Imaginary part of the self-energy near the fermi-surface from self-consistent parquet DΓA and ladder DΓA [54] in the ph-channel at $U = 4t$ and half filling.

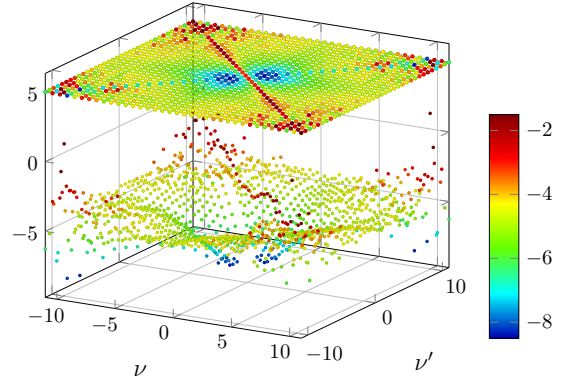
3.2.2 Comparison of methods

Qualitatively, the results of the self-consistent parquet DΓA and the one-shot parquet DΓA have been found to be similar to the results of the parquet approximation for the 2D Hubbard model at the Coulomb interaction and temperature considered. This is shown in Fig. 3.10. The difference between the methods becomes visible in the structure of the generated non-local vertices. Fig. 3.12 compares the non-local magnetic irreducible vertices from parquet approximation and DΓA and gives the corresponding local vertices

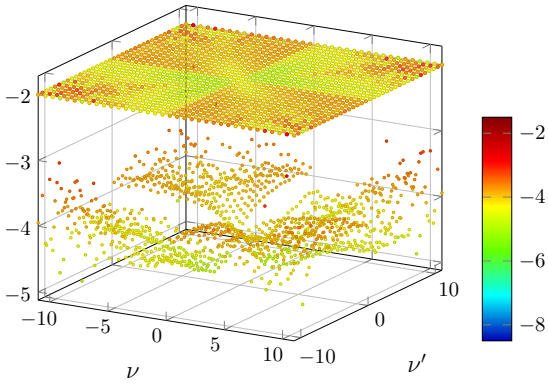
$\Gamma_m^{PA}(\nu, \nu', \omega = 0)$ at $\mathbf{k} = \mathbf{k}' = (0, 0)$ and $\mathbf{q} = (\pi, \pi)$



$\Gamma_m^{D\Gamma A}(\nu, \nu', \omega = 0)$ at $\mathbf{k} = \mathbf{k}' = (0, 0)$ and $\mathbf{q} = (\pi, \pi)$



$\Lambda_m^{DMFT}(\nu, \nu', \omega = 0)$



$\Gamma_m^{DMFT}(\nu, \nu', \omega = 0)$

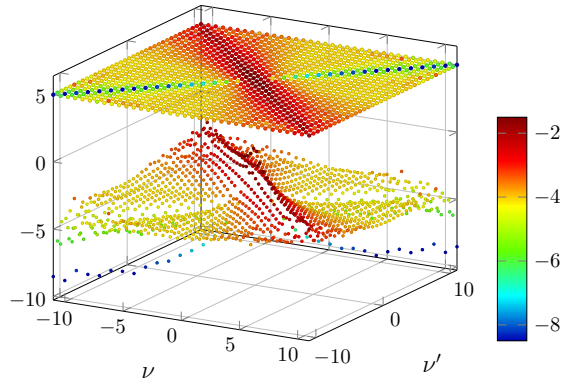


Figure 3.12: Irreducible vertex generated in the parquet Approximation [52] (top left) and the self-consistent parquet DΓ A (top right). Bottom left: The fully irreducible vertex from DMFT that served as input for the parquet DΓ A. Bottom right: The corresponding magnetic irreducible vertex from the impurity. All at $\beta t = 10, U = 4t$ and half filling.

Γ_m and Λ from DMFT.

The difference between the parquet DΓ A and the ladder DΓ A is much more pronounced, as shown in Fig. 3.11 for the self-energy. The pseudogap, which was not found in the parquet DΓ A yet at all, develops at much higher temperatures in the ladder DΓ A and can be identified by the sharp downturn (divergence) of $\Im(\Sigma)$ in Fig 3.11. Note that in the ladder DΓ A the non-local vertices and the susceptibility are not generated at all in one of the channels, in this case the pp -channel. This has to be taken into account when comparing the methods in that respect.

3.2.2.1 Effect of the outer self-consistency

Fig. 3.13 shows the effect of the outer self-consistency on the self-energy for a variety of parameters. All calculations were done on a 6×6 cluster and the self-energy is given on two points near the Fermi surface, $(0, \pi)$ and $(\frac{2\pi}{6}, \frac{4\pi}{6})$, as well as the point $(0, 0)$. Note that, due to the small cluster size, these are the only two independent \mathbf{k} -points near the Fermi surface that are not related to another one through symmetry. It is clear that the corrections from the outer self-consistency are most pronounced near half-filling and almost non-existent in the doped case at $U = 4t$. Also, they seem to be enhanced with larger interaction as may be inferred from comparing the lower two plots. There are no results for larger filling at that interaction, however, because the Bethe-Salpeter equations diverge for this limited system size. In the accessible parameter range, no qualitative difference, such as the establishment of a pseudogap, was found between the results from the one-shot and self-consistent scheme. For larger interaction and lower temperatures, the corrections to the local Green's function stemming from non-local correlations may be expected to be larger due to the proximity to the superconducting instability. The outer self-consistency may then be expected to have a larger effect than in the current cases. Fig. 3.14 shows the change in the fully irreducible vertex from DMFT to self-consistent parquet D Γ A in the case where the effect of the outer-self consistency was most pronounced, $\beta t = 20, U = 4t, n = 1$.

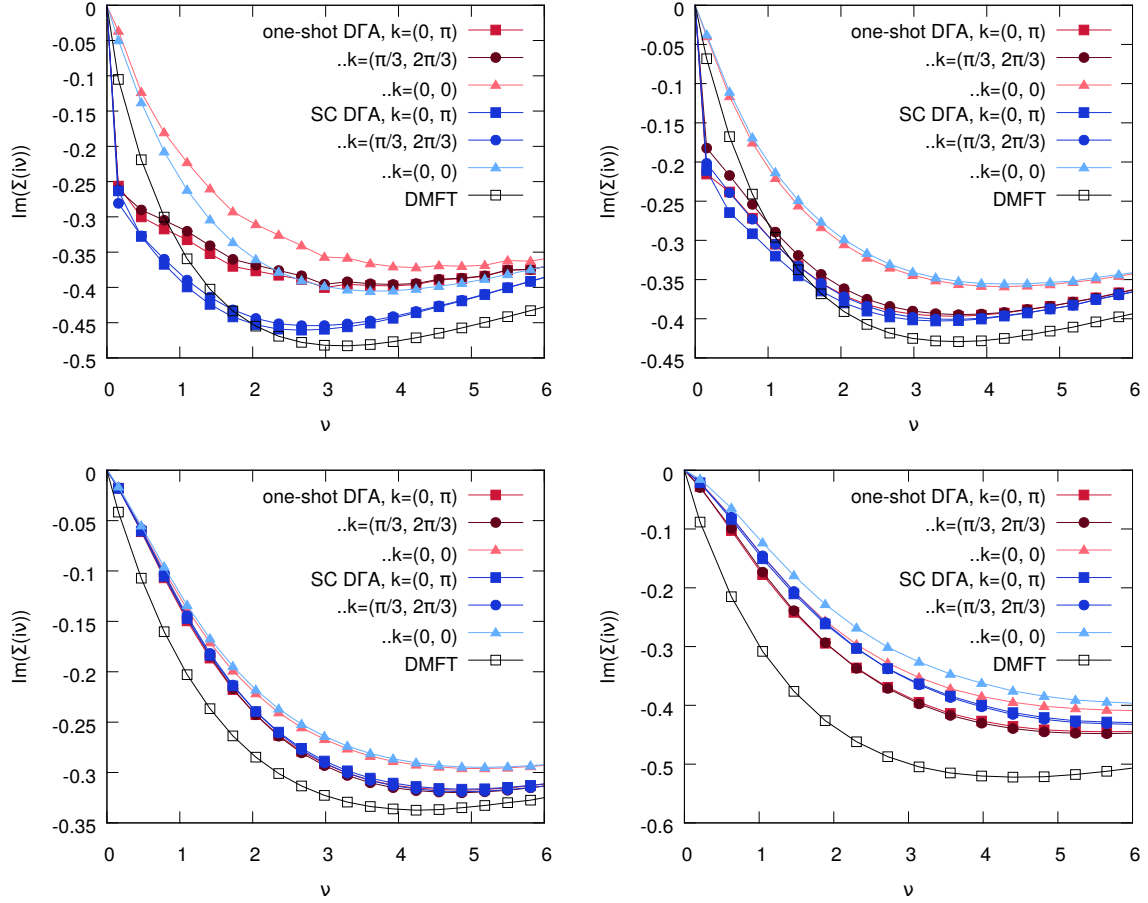


Figure 3.13: Imaginary part of the self-energy as obtained from self-consistent and one-shot parquet DΓA as well as DMFT, for $\beta t = 20$, $U = 4t$, $n = 1$ (top left), $n = 0.85$ (top right) and $n = 0.7$ (bottom left) and the same for $\beta t = 15$, $U = 5t$, $n = 0.7$ (bottom right).

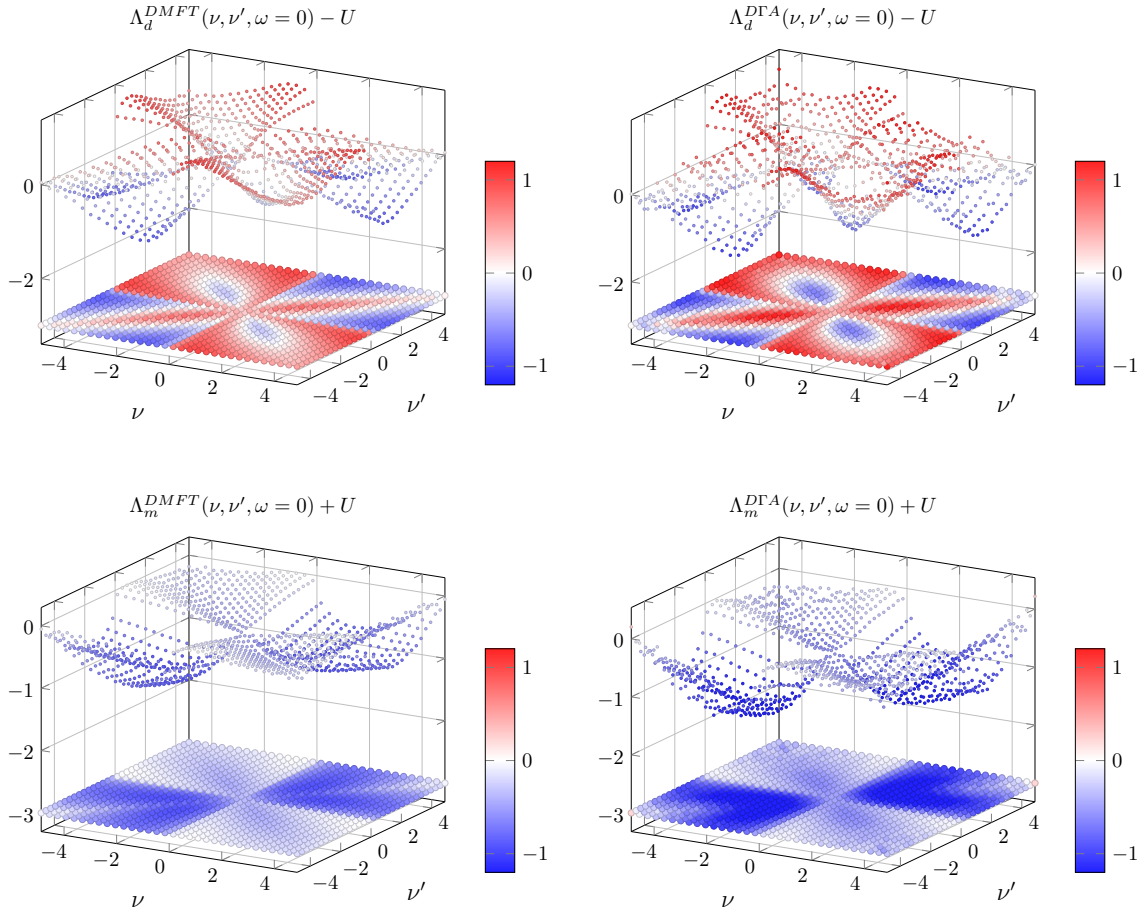


Figure 3.14: Change in Λ_d and Λ_m from DMFT (left) to the self-consistent parquet DΓA (right) at $\beta t = 20, U = 4t, n = 1$.

3.2.3 Computational cost

The by far most expensive part in the fully self-consistent parquet D Γ A is the solution of the parquet equations. The limiting factor is memory consumption as the size of the vertices scales as the third power of frequency range and, in two dimensions, the sixth power of the cluster size $N_{\mathbf{k}}$. The calculations were done on the Vienna Scientific Cluster VSC-3 on machines with two Intel Xeon E5-2650v2, 2.6 GHz processors with 8 cores each and 64 GB of RAM. Due to the limited memory, the calculation for the parquet equations had to be spread out over several nodes without being able to use all 16 cores on each one of them for larger N_{ω} and $N_{\mathbf{k}}$. For the CT-QMC calculations, where memory is not an issue, all 16 cores were used. The following table compares the computational resources spent for some of the calculations done during this work, each given for one iteration of D Γ A, that is from the update of Λ to the solution of the parquet equations using that same Λ . Depending on the desired accuracy in the statistics of the Monte-Carlo calculations and the convergence criterion for the parquet equations, these values may vary significantly.

			Parquet equations					CT-QMC (CPU-h)	
β	U	$\langle n \rangle$	N_{ω}	$N_{\mathbf{k}} \times N_{\mathbf{k}}$	CPU-h	RAM	cores used	inv. AIM	Λ_{AIM}
10	4	1	32	6×6	1,000	520 GB	8/16	500	1,000
20	4	1	48	6×6	25,000	1.8 TB	2/16	1,000	5,000
20	4	0.7	48	6×6	20,000	1.8 TB	2/16	1,000	5,000
5	4	1	32	8×8	15,000	3.0 TB	2/16	500	1,000
20	4	1	32	8×8	30,000	3.0 TB	2/16	1,000	5,000

3.2.4 Convergence

The self-consistent solution of the parquet equations (inner self-consistency) fails to converge for $\beta t \gtrsim 20$ and $U \gtrsim 5$. Depending on the parameters and the filling, convergence may take upwards of 150 iterations of the parquet equations. For large interaction, the Bethe-Salpeter equation may even diverge in the magnetic channel. Notably, the parquet D Γ A fails to converge already at higher temperatures than the parquet approximation. For example, at $\beta t = 20, U = 5t, n = 1$, the parquet approximation with $\Lambda = U$ converges, while parquet D Γ A with $\Lambda = \Lambda_{DMFT}$ does not. Convergence is improved with a larger cluster, so there is hope to go to lower temperatures in the future. Once a solution of the one-shot parquet D Γ A was found, the outer self-consistency converged at all parameter sets. This took approximately 10 iterations at half filling and even less away from half filling where the effect of the outer self-consistency was even smaller.

Chapter 4

Conclusion and outlook

The implementation of the parquet D Γ A has only recently become feasible with the development of a new and powerful parquet-solver, the `victory-code` [26]. In this work, we presented the formalism and the steps to a self-consistent parquet D Γ A solution. After introducing the underlying formulas, we gave special focus to the calculation of the fully irreducible vertex on the impurity, a key component of the parquet D Γ A. We discussed the possibility of using Kernel-functions [33] for an improved calculation of the high-frequency asymptotics of the fully irreducible vertex Λ . While this method has proven valuable in the calculation of the irreducible vertices Γ that enter, for example, the ladder D Γ A, we found no benefit in applying it to our problem of calculating Λ . This was not a real setback to the implementation of the parquet D Γ A however, as the inevitable noise in the impurity calculations can relatively cheaply be kept sufficiently low to not impact the solution of the parquet equations. We further showed a method to update the auxiliary impurity model in order to achieve the outer self-consistency and made an attempt to show the uniqueness of the solution of that step.

The outer self-consistency was found to be particularly important in the case of the benzene molecule, where non-local interactions were introduced according to the Pariser-Parr-Pople model [42]. In the two-dimensional Hubbard model, the feedback of non-local correlations into the local one-particle Green's function provided by the outer self-consistency did not have a big impact for the currently accessible parameter sets. This may change once parameters closer to the superconducting instability are feasible. Temperature and interaction strength are currently limited by the convergence of the parquet equations, which can be expected to behave better with larger cluster sizes. Moreover, for lower temperatures more Matsubara frequencies will have to be taken into account, further increasing the already heavy memory consumption. Due to the unfavorable scaling of the size of the vertices with the number of frequencies and, even more so, the clus-

ter size, new ways to decrease the computational demand will be highly welcome. One method proposed for this purpose is the use of so-called form-factors for a more efficient parametrization of the fermionic momenta [55]. Even at the accessible parameters, which are relatively far from a possible superconducting instability, a range of interesting quantities can be extracted from the non-local vertices. These results have already indicated possible $d_{x^2-y^2}$ ordering in the two-dimensional Hubbard model, as well as an unexpected \tilde{s} -wave pairing.

Still, the path to realistic multi-orbital calculations within the parquet D Γ A is long and certainly will give rise to many interesting challenges along the way. The method, however, has already proven to give good results from a natural and elegant approximation.

Bibliography

- [1] J. Hubbard. Electron correlations in narrow energy bands. *The Royal Society*, pages 238–257 (1963).
- [2] N. F. Mott. Metal-Insulator Transition. *Rev. Mod. Phys.*, 40, 677 (1968). 10.1103/RevModPhys.40.677.
- [3] T. Maier, M. Jarrell, T. C Schulthess, P. Kent, and J. B White. Systematic Study of d -Wave Superconductivity in the 2D Repulsive Hubbard Model. 95, 237001 (2006).
- [4] A. Georges, G. Kotliar, W. Krauth, and M. J. Rozenberg. Dynamical mean-field theory of strongly correlated fermion systems and the limit of infinite dimensions. *Rev. Mod. Phys.*, 68, 13 (1996). 10.1103/RevModPhys.68.13.
- [5] E. Gull, A. J. Millis, A. I. Lichtenstein, A. N. Rubtsov, M. Troyer, and P. Werner. Continuous-time Monte Carlo methods for quantum impurity models. *Reviews of Modern Physics*, 83, 349 (2011). 10.1103/RevModPhys.83.349. 1012.4474.
- [6] P. W. Anderson. The Resonating Valence Bond State in La₂CuO₄ and Superconductivity. *Science*, 235, 1196 (1987).
- [7] K. Held. Dynamical Vertex Approximation. *ArXiv e-prints* (2014). 1411.5191.
- [8] A. Toschi, A. A. Katanin, and K. Held. Dynamical vertex approximation: A step beyond dynamical mean-field theory. *Phys. Rev. B*, 75, 045118 (2007). 10.1103/PhysRevB.75.045118.
- [9] G. Rohringer, H. Hafermann, A. Toschi, A. A. Katanin, A. E. Antipov, M. I. Katsnelson, A. I. Lichtenstein, A. N. Rubtsov, and K. Held. Diagrammatic routes to non-local correlations beyond dynamical mean field theory. *ArXiv e-prints* (2017). 1705.00024.
- [10] L. Landau and E. M. Lifshitz. *Theory of the Condensed State*, pages 173–222. Pergamon Press (1981).

- [11] A.-M. Tremblay. Strongly Correlated Superconductivity. Autumn School on Correlated Electrons (2013).
- [12] D. J. Scalapino. The case for $d_{x^2-y^2}$ Pairing in the Cuprate Superconductors. *Physics Reports*, 250, 047005 (1995).
- [13] W. Metzner. Superconductivity in the Two-Dimensional Hubbard Model. *Foundations of Physics*, 30(12), 2101 (2000). 10.1023/A:1003793524858.
- [14] N. Bulut, D. Scalapino, and S. White. Spin-fluctuation mediated interaction in the two-dimensional Hubbard model. *Physica C: Superconductivity*, 246(1), 85 (1995). [https://doi.org/10.1016/0921-4534\(95\)00130-1](https://doi.org/10.1016/0921-4534(95)00130-1).
- [15] C. Tsuei and J. Kirtley. Pairing symmetry in cuprate superconductors. *Reviews of Modern Physics*, 72(4) (2000).
- [16] O. Gunnarsson, M. W. Haverkort, and G. Sangiovanni. Analytical continuation of imaginary axis data using maximum entropy. *Phys. Rev. B*, 81(15), 155107 (2010). 10.1103/PhysRevB.81.155107. 1001.4351.
- [17] G. D. Mahan. *Green's Functions at Finite Temperatures*, pages 123–220. Plenum Press (1986).
- [18] J. Imriska. *Hubbard models on general lattices. A dynamical cluster approximation approach*. Ph.D. thesis, ETH Zürich (2016).
- [19] G. Rohringer. *New routes towards a theoretical treatment of nonlocal electronic correlations*. Ph.D. thesis, TU Wien (2013).
- [20] P. W. Anderson. Localized Magnetic States in Metals. *Phys. Rev.*, 124, 41 (1961). 10.1103/PhysRev.124.41.
- [21] P. Werner and A. J. Millis. Hybridization expansion impurity solver: General formulation and application to Kondo lattice and two-orbital models. *Phys. Rev. B*, 74, 155107 (2006). 10.1103/PhysRevB.74.155107.
- [22] M. Wallerberger, A. Hausoel, P. Gunacker, A. Kowalski, N. Parragh, F. Goth, K. Held, and G. Sangiovanni. w2dynamics: Local one- and two-particle quantities from dynamical mean field theory. *ArXiv e-prints* (2018). 1801.10209.
- [23] N. Parragh, M. Wallerberger, A. Hausoel, P. Gunacker, A. Kowalski, and G. Sangiovanni. w2dynamics. Code release in preparation.

- [24] P. Gunacker, M. Wallerberger, E. Gull, A. Hausoel, G. Sangiovanni, and K. Held. Continuous-time quantum Monte Carlo using worm sampling. *Phys. Rev. B*, 92, 155102 (2015). 10.1103/PhysRevB.92.155102.
- [25] P. Gunacker. *Diagrammatic Quantum Monte Carlo with Worm Sampling*. Master’s thesis, TU Wien (2014).
- [26] G. Li, A. Kauch, P. Pudleiner, and K. Held. The victory project v1.0: an efficient parquet equations solver. *ArXiv e-prints* (2017). 1708.07457.
- [27] T. A. Maier, M. S. Jarrell, and D. J. Scalapino. Structure of the Pairing Interaction in the Two-Dimensional Hubbard Model. *Physical Review Letters*, 96(4), 047005 (2006). 10.1103/PhysRevLett.96.047005. cond-mat/0508361.
- [28] N. E. Bickers. *Self-Consistent Many-Body Theory for Condensed Matter Systems*, pages 237–296. Springer New York, New York, NY (2004).
- [29] K. Held, C. Taranto, G. Rohringer, and A. Toschi. Hedin Equations, GW, GW+DMFT, and All That. Autumn School on Correlated Electrons (2011).
- [30] A. Zagoskin. *Quantum Theory of Many-Body Systems: Techniques and Applications*. Springer, London (2014).
- [31] S. Kurth. Introduction to Green functions, the GW approximation, and the Bethe-Salpeter equation. University Lecture (2015).
- [32] J. Kaufmann, P. Gunacker, and K. Held. Continuous-time quantum Monte Carlo calculation of multiorbital vertex asymptotics. *Phys. Rev. B*, 96(3), 035114 (2017). 10.1103/PhysRevB.96.035114. 1703.09407.
- [33] N. Wentzell, G. Li, A. Tagliavini, C. Taranto, G. Rohringer, K. Held, A. Toschi, and S. Andergassen. High-frequency asymptotics of the vertex function: diagrammatic parametrization and algorithmic implementation. *ArXiv e-prints* (2016). 1610.06520.
- [34] J. Kaufmann. *Calculation of Vertex Asymptotics from Local Correlation Functions*. Master’s thesis, TU Wien (2017).
- [35] G. Rohringer, A. Valli, and A. Toschi. Local electronic correlation at the two-particle level. *Phys. Rev. B*, 86(12), 125114 (2012). 10.1103/PhysRevB.86.125114. 1202.2796.

- [36] G. Li, N. Wentzell, P. Pudleiner, P. Thunström, and K. Held. Efficient implementation of the parquet equations: Role of the reducible vertex function and its kernel approximation. *Phys. Rev. B*, 93(16), 165103 (2016). 10.1103/PhysRevB.93.165103. 1510.03330.
- [37] S. X. Yang, H. Fotso, J. Liu, T. A. Maier, K. Tomko, E. F. D’Azevedo, R. T. Scalettar, T. Pruschke, and M. Jarrell. Parquet approximation for the 4×4 Hubbard cluster. *Phys. Rev. E*, 80(4), 046706 (2009). 10.1103/PhysRevE.80.046706. 0906.4736.
- [38] K.-M. Tam, H. Fotso, S.-X. Yang, T.-W. Lee, J. Moreno, J. Ramanujam, and M. Jarrell. Solving the parquet equations for the Hubbard model beyond weak coupling. *Phys. Rev. E*, 87(1), 013311 (2013). 10.1103/PhysRevE.87.013311. 1108.4926.
- [39] M. Jarrell, T. Maier, C. Huscroft, and S. Moukouri. Quantum Monte Carlo algorithm for nonlocal corrections to the dynamical mean-field approximation. *Phys. Rev. B*, 64(19), 195130 (2001). 10.1103/PhysRevB.64.195130. cond-mat/0108140.
- [40] L. Boehnke, H. Hafermann, M. Ferrero, F. Lechermann, and O. Parcollet. Orthogonal polynomial representation of imaginary-time Green’s functions. *Phys. Rev. B*, 84(7), 075145 (2011). 10.1103/PhysRevB.84.075145. 1104.3215.
- [41] T. Schäfer. *Classical and quantum phase transitions in strongly correlated electron systems*. Ph.D. thesis, TU Wien (2016).
- [42] R. Pariser and R. G. Parr. A Semi-Empirical Theory of the Electronic Spectra and Electronic Structure of Complex Unsaturated Molecules. I. *Journal of Chemical Physics*, 21, 466 (1953). 10.1063/1.1698929.
- [43] A. Galler, P. Thunström, P. Gunacker, J. M. Tomczak, and K. Held. Ab initio dynamical vertex approximation. *Phys. Rev. B*, 95, 115107 (2017). 10.1103/PhysRevB.95.115107.
- [44] P. Pudleiner. In preparation.
- [45] N. Bulut. $d_{x^2-y^2}$ superconductivity and the Hubbard Model. *Advances in Physics*, 51(7), 1587 (2002).
- [46] D. J. Scalapino. A common thread: The pairing interaction for unconventional superconductors. *Reviews of Modern Physics*, 84, 1383 (2012). 10.1103/RevModPhys.84.1383. 1207.4093.

- [47] J. Kunes. Efficient treatment of two-particle vertices in dynamical mean-field theory. *Phys. Rev. B*, 83(8), 085102 (2011). 10.1103/PhysRevB.83.085102. 1010.3809.
- [48] N. D. Mermin and H. Wagner. Absence of Ferromagnetism or Antiferromagnetism in One- or Two-Dimensional Isotropic Heisenberg Models. *Phys. Rev. Lett.*, 17, 1133 (1966). 10.1103/PhysRevLett.17.1133.
- [49] X. Chen, J. P. F. LeBlanc, and E. Gull. Superconducting Fluctuations in the Normal State of the Two-Dimensional Hubbard Model. *Physical Review Letters*, 115(11), 116402 (2015). 10.1103/PhysRevLett.115.116402. 1507.04475.
- [50] P. Werner, E. Gull, O. Parcollet, and A. J. Millis. Momentum-selective metal-insulator transition in the two-dimensional Hubbard model: An 8-site dynamical cluster approximation study. *Phys. Rev. B*, 80, 045120 (2009). 10.1103/PhysRevB.80.045120.
- [51] M. Kitatani, T. Schäfer, H. Aoki, and K. Held. Why T_c is so low in high- T_c cuprates: importance of the dynamical vertex structure. *ArXiv e-prints* (2018). 1801.05991.
- [52] A. Kauch. Personal communication, January 2018.
- [53] E. Berg, E. Fradkin, S. A. Kivelson, and J. M. Tranquada. Striped superconductors: how spin, charge and superconducting orders intertwine in the cuprates. *New Journal of Physics*, 11(11), 115004 (2009).
- [54] M. Kitatani, T. Schäfer, H. Aoki, and K. Held. ladder DGA (2018). Unpublished.
- [55] J. Lichtenstein, D. Sánchez de la Peña, D. Rohe, E. Di Napoli, C. Honerkamp, and S. A. Maier. High-performance functional Renormalization Group calculations for interacting fermions. *Computer Physics Communications*, 213, 100 (2017). 10.1016/j.cpc.2016.12.013. 1604.06296.

Acknowledgements

First of all, I want to thank Karsten Held for giving me the opportunity to work on such an exciting project and entrusting me with the CPU-hours to complete it. Within several lectures and especially during the work on this thesis, he has created some of the most enlightening moments of my studies.

My special thanks goes to Anna Kauch. Her patience, time and advice have kept my motivation high throughout the work on this thesis, and without her insights it certainly would not have been possible.

I also want to acknowledge the direct support from Patrik Gunacker, Josef Kaufmann, Daniel Springer and Petra Pudleiner, as well as the generally great atmosphere in Karsten Held's group and among my fellow office inhabitants.

For their moral support, I especially want to thank Sheila Tello, my brothers Christian and Stephan and my sister Karoline, as well as the newcomers Julian and Paula.

Finally, this thesis would be incomplete without expressing my deepest gratitude towards my parents, Josef and Pauline, for their unlimited support throughout the years.